



HAL
open science

HIV-induced membraneless organelles orchestrate post-nuclear entry steps

Viviana Scoca, Marion Louveaux, Renaud Morin, Dmitry Ershov, Jean-Yves Tinevez, Francesca Di Nunzio

► **To cite this version:**

Viviana Scoca, Marion Louveaux, Renaud Morin, Dmitry Ershov, Jean-Yves Tinevez, et al.. HIV-induced membraneless organelles orchestrate post-nuclear entry steps. 2021. pasteur-03214329v2

HAL Id: pasteur-03214329

<https://pasteur.hal.science/pasteur-03214329v2>

Preprint submitted on 1 May 2021

HAL is a multi-disciplinary open access archive for the deposit and dissemination of scientific research documents, whether they are published or not. The documents may come from teaching and research institutions in France or abroad, or from public or private research centers.

L'archive ouverte pluridisciplinaire **HAL**, est destinée au dépôt et à la diffusion de documents scientifiques de niveau recherche, publiés ou non, émanant des établissements d'enseignement et de recherche français ou étrangers, des laboratoires publics ou privés.

Copyright

HIV-induced membraneless organelles orchestrate post-nuclear entry steps.

Viviana Scoca^{1,2}, Marion Louveau^{*3,4}, Renaud Morin^{*5}, Dmitry Ershov^{4,6}, Jean-Yves Tinevez⁴, Francesca Di Nunzio¹

¹Department of Virology, Advanced Molecular Virology and Retroviral Dynamics Group, Pasteur Institute, Paris, France

²BioSPC Doctoral School, Université de Paris, Paris, France

³Department of Cell Biology and Infection, Biological Image Analysis, Pasteur Institute, Paris, France

⁴Image Analysis Hub/ C2RT, Pasteur Institute, Paris, France

⁵Imactiv-3D, 1 Place Pierre Potier, 31106 Toulouse, France

⁶Department of Computational Biology, Hub of Bioinformatics and Biostatistics, Pasteur Institute, USR 3756 CNRS, Paris, France.

*equal contribution

Running title: Deciphering the host nucleus subversion by HIV-1 to replicate.

Abstract

HIV integration occurs in chromatin sites that favor the release of high levels of viral progeny, alternatively the virus is also able to coexist discreetly with the host. To uncover the HIV-1 DNA fate in the nuclear landscape, we directly tracked the viral DNA and the viral RNA by coupling HIV-1 ANCHOR technology with RNA FISH or MCP-MS2 RNA-tagging bacterial system. Our computational imaging analysis revealed that proviral forms are early located in proximity of the nuclear periphery of mitotic and non-mitotic cells. HIV-1 triggers the nuclear clustering of the host factor CPSF6, but yet its role is poorly understood. Our data show that CPSF6 clusters are part of HIV-induced membraneless organelles (HIV-1 MLOs). Interestingly, we observed that viral genomic RNAs and the integrase proteins are sequestered in CPSF6 clusters, in which the virus can reverse transcribe, while the late retrotranscribed DNA is excluded from these structures. HIV-1 MLOs are formed in the interchromatin space, indicating that they are not proviral sites, but orchestrate viral events prior to the integration step. We found transcription-competent proviruses localize outside HIV-1 MLOs, in LEDGF-abundant regions, known to be active chromatin sites. This study highlights single functional host-proviral complexes in their nuclear landscape, which is markedly restructured by HIV-1 to favor viral replication.

38

39 **Introduction**

40 Immediately after fusion at the plasma membrane, HIV-1 cores are released into the
41 cytoplasm and move towards the nucleus, while the viral RNA (vRNA) genome begins
42 the process of reverse transcription (RT) into double-stranded DNA (dsDNA)
43 (Campbell and Hope, 2015; Di Nunzio, 2013; Scoca and Di Nunzio, 2021a). Once
44 imported in the nucleus, the interplay between the HIV-1 DNA genome and the host
45 chromatin compartment is crucial for the fate of the virus-host coexistence. HIV-1 can
46 adopt either an episomal or a proviral form (Butler et al., 2001). The fate of these viral
47 DNA (vDNA) forms and their surrounding chromatin landscape dictate the evolution of
48 HIV infection (Maldarelli, 2016; Sharkey et al., 2011; Sharkey et al., 2000). The
49 mechanisms determining the fate of the proviral DNA in the nucleus are still under
50 investigation (Liu et al., 2020; Olson et al., 2019) also because of the limits imposed
51 by available technologies. Real-time imaging approaches provide new insight into
52 unprecedented spatial information of individual HIV-1 infected cells. Several strategies
53 have enabled the visualization of the viral components during nuclear entry to indirectly
54 track the HIV-1 pre-integration complex (PIC) : Integrase (IN)-TC/FIAsH, APOBEC 3F
55 (A3F)-YFP, IN-YFP, Gag-iGFP, Cyclophilin A (CypA)-DsRed/ Capsid (CA), INsfGFP,
56 and CA-GFP (Burdick et al., 2017; Hubner et al., 2009; Lelek et al., 2012) (Francis et
57 al., 2016; Francis and Melikyan, 2018) (Mamede et al., 2017) (Albanese et al., 2008;
58 Francis et al., 2014). Recent new discoveries in the field shed light on the central role
59 of the viral capsid in leading the viral genome in the host nucleus (Blanco-Rodriguez
60 et al., 2020; Burdick et al., 2020), contrary to what was widely believed (Farnet and
61 Haseltine, 1991; Suzuki and Craigie, 2007). The viral nuclear translocation is dictated
62 by the capsid interplay with host factors, such as Cleavage and polyadenylation
63 specificity factor subunit 6 (CPSF6)(Buffone et al., 2018; Lee et al., 2010; Price et al.,
64 2014), which is a paraspeckle factor (Fox et al., 2002; Naganuma and Hirose, 2013)
65 and Nup153 (Di Nunzio et al., 2013; Lelek et al., 2015). CPSF6, vDNA, vRNA and
66 transcription factors have been found in nuclear speckles (NSs), suggesting that their
67 co-appearance is consistent with productive integration in these nuclear bodies
68 (Francis et al., 2020; Stultz et al., 2017). Interestingly, CPSF6 contains intrinsically
69 disordered mixed-charge domains which are responsible for the formation of liquid
70 condensates *in vitro* (Greig et al., 2020) and they may account for the remodeling of
71 membraneless organelles (MLOs) in infected cells (Scoca and Di Nunzio, 2021b).

72 However, although NSs contain viral components they are by definition interchromatin
73 granules (Lamond and Spector, 2003), thus they cannot be HIV-1 integration sites.
74 Thus, the specific role of these host/viral nuclear organelles remain unclear. Of note,
75 mechanisms underlying viral post-nuclear entry steps and the role of nuclear structures
76 induced by HIV-1 during viral replication could be revealed only by the direct co-
77 labeling of vDNA forms and host factors. Thus far, all vDNA forms from the early to the
78 late RT products can be indistinguishably visualized in fixed cells, either by supplying
79 5-Ethynyl-2'-deoxyuridine (EdU) during infection (Peng et al., 2014; Rensen et al.,
80 2020), which is limited to non-dividing cells (De Wit et al., 2019) or by DNA-FISH
81 (Marini et al., 2015) or bDNA (Chin et al., 2015). However, the exclusive labeling of
82 late reverse transcribed DNA products in fixed and in live cells is challenging but
83 important, because they are the only vDNA forms included in the mature PIC.

84 Here, we were able to specifically live track the late reverse transcribed DNA as
85 episomal or as proviral forms, showing their divergent intranuclear behavior. In parallel,
86 we detect the location of functional proviruses in the nuclear space of the main target
87 cells of the virus, such as CD4⁺T cells and macrophages, by using HIV-1 ANCHOR
88 methodology (Blanco-Rodriguez et al., 2020) to label the vDNA and RNA FISH or the
89 MCP-MS2 system (Tantale et al., 2016) to identify the vRNA foci. Next, we deepened
90 the study of the nuclear landscape that surrounds proviruses. We observed that viral
91 infection reprogramed the nuclear location of CPSF6, building HIV-1 membraneless
92 organelles (HIV-1 MLOs). Our data emphasize post nuclear entry steps finely
93 regulated by the interplay between viral and host components. In particular, we
94 investigated whether HIV-1 MLOs could be physiological sites of nuclear reverse
95 transcription, as well as maturation centers of HIV-1 PIC. We found that HIV-1 MLOs
96 are enlarged NSs and constitute microenvironments favorable for HIV-1 PIC
97 maturation. In addition, we observed foci of viral replication excluded but in the vicinity
98 of HIV-1 MLOs and of the nuclear envelope (NE). Of note, our results indicate that
99 HIV-1 DNA localization is key to identifying partners of HIV-1 that aid the virus to hijack
100 cellular mechanisms to persist in the host cells and to highlight the nuclear landscape
101 surrounding single viral genomes. Our study provides new insights into how HIV
102 reprograms and markedly restructures the nuclear environment to orchestrate viral
103 replication steps.

104 **Results**

105 **Live tracking of HIV-1 DNA forms in the nucleus of target cells.**

106 With the aim of studying HIV-1 DNA nuclear fate in different cell types, we benefited of
107 the HIV-1 ANCHOR DNA labeling system (Fig. 1A) (Blanco-Rodriguez et al., 2020).
108 Once fully retrotranscribed, the HIV-1 genome carrying the bacterial sequence ANCH3
109 is specifically recognized by OR-GFP protein, which is expressed in the target cells,
110 genetically modified by the lentiviral vector (LV) OR-GFP (Blanco-Rodriguez et al.,
111 2020). The accumulation of OR-GFP, which is a modified version of the bacterial ParB
112 protein (Graham et al., 2014; Sanchez et al., 2015), on the ANCH3 sequence
113 generates bright nuclear signals (Fig.1A). Importantly, OR protein binds exclusively the
114 double stranded DNA (Saad et al., 2014). We cloned ANCH3 in the nef gene, thus,
115 HIV-1 ANCHOR system exclusively detects late reverse transcripts, because the
116 ANCH3 sequence is one of the last sequences to be converted into double stranded
117 DNA (Fig. 1A). Therefore, the HIV-1 ANCHOR approach allows only the visualization
118 of potential functional vDNA. Since the HIV-1 genome dissociates from viral proteins
119 to become a proviral DNA or an extrachromosomal DNA, the track of these viral forms
120 is the only direct measurement to investigate the fate of the viral genome into the host
121 nuclear space. Unlike previous studies (Burdick et al., 2017; Burdick et al., 2020; Chin
122 et al., 2015; Francis et al., 2020; Francis and Melikyan, 2018), we are now able to
123 directly visualize by live imaging the nuclear vDNA as GFP puncta appearing in the
124 host nucleus once retrotranscribed (Fig. 1A). HIV-1 ANCHOR is able to specifically
125 label the vDNA as shown by the correlation between the nuclear GFP puncta and the
126 MOI (multiplicity of infection) used (Fig. S1A). This specificity was corroborated using
127 the reverse transcription inhibitor, Nevirapine (NEV), which completely prevents the
128 detection of vDNA (Fig. 1B, Fig.S1B). We then investigated whether HIV-1 ANCHOR
129 allows the detection of different intranuclear vDNAs, such as episomal and integrated
130 forms. To generate episomal forms, either we infected cells with HIV-1 ANCH3 in the
131 presence of the integration inhibitor Raltegravir (RAL), or using an integration-deficient
132 virus, which is mutated at the catalytic site of the integrase (IN) enzyme (HIV-1 ANCH3
133 IN_{D116A}). We detected intranuclear GFP puncta under both conditions (Fig. 1B),
134 meaning that HIV-1 ANCHOR permits the detection of nuclear episomal vDNA forms.
135 The experiments were validated by qPCR, which confirmed the extrachromosomal
136 forms generated during infection when the integration step is impeded (Fig. 1B). We

137 next assessed whether HIV-1 ANCHOR is sufficiently sensitive to allow the detection
138 of integrated vDNA at the level of a single provirus. We selected single HeLa P4R5
139 clones carrying the HIV-1 ANCH3 genome. The imaging data correlates with results
140 obtained by ALU PCR (Fig. 1C), demonstrating that this technology is powerful enough
141 to detect a single provirus. Thus, we used this system to live track both proviruses and
142 episomal forms to investigate their behaviour in the nucleus (video 1, 2, and 3). We
143 performed live tracking of vDNAs in cells at six days post infection (p.i.) (video 1), which
144 contain a negligible amount of episomal forms, likely lost during cell division (Fig. S1C),
145 in the single-cell clone (video 2) or in cells containing only the episomal vDNA (video
146 3). Then, we compared vDNA trajectories in the aforementioned experimental
147 conditions (Fig. 1D). The stable clone and the cells at six days p.i. show vDNA with
148 similar trajectories and diffusion coefficient (D (nm²/s) < 5). Instead, infected cells
149 carrying unintegrated viruses harbored two populations composed of episomal forms
150 with divergent behaviors, one with a low D (D (nm²/s) < 5) and the other with a high D
151 ($5 < D$ (nm²/s) < 20) (Fig. 1D). Our data hint that most, but not all, episomal forms are
152 retained in particular nuclear regions, most likely interacting with host factors or
153 chromatin compartments, consistent with the findings of other studies (Geis and Goff,
154 2019; Zhu et al., 2018), whereas some episomal forms are free to move in the nuclear
155 space. On the other hand, the integrated forms showed a uniform, low-diffusive
156 behavior.

157

158 **Detection of actively transcribing proviruses at single-cell level in HIV-1 target** 159 **cells.**

160 The identification of the functional vDNA in the nucleus of infected cells has been one
161 of our goals. For this purpose, we combined HIV-1 ANCHOR technology with RNA
162 FISH (single molecule inexpensive FISH, smiFISH) against HIV-1 polymerase
163 transcripts, to detect vRNA foci of transcription (Tsanov et al., 2016), using ethanol
164 treatment and 5h of probe hybridization (Fig. S4). As expected, in cells treated with
165 RAL, where the integration step is blocked, vRNA signal is highly depleted. In
166 untreated cells it is possible to observe vDNA-vRNA associations, highlighting the
167 proviruses location (Fig. 2A), in fact proviruses are the only transcribing forms. We
168 strengthen our results on the ability to visualize proviruses by showing the vDNA-vRNA
169 association by live imaging. HIV-1 transcriptional activity was tracked by MCP-GFP
170 system (kind gift from E. Bertrand) to label the vRNA (Tantale et al., 2016) coupled

171 with HIV-1 ANCHOR technology (Fig. S2A and B). Next, we compared the intensity of
172 ANCHOR signals of the episomal forms (+ RAL) with those of the integrated forms (-
173 RAL) and observed that the signal of unintegrated DNA was two-fold brighter than the
174 proviral DNA spot (Fig. 2A) in HeLa cells. Interestingly, we also remarked, during live
175 imaging, that the vDNA of the integration-deficient virus (HIV-1 ANCH3 IN_{D116A})
176 clusters in the nucleus (Fig. S2C, video 4). Aggregation of extrachromosomal forms
177 could prompt a brighter appearance of viral episomal DNA compared to a dimmer
178 signal of the individual proviral DNA (Fig. 2A), at least in HeLa cells. Next, we
179 pinpointed transcriptionally active proviruses in the main HIV-1 target cells, CD4⁺ T
180 cells and macrophages, by co-detecting vRNA and vDNA (Fig. 2 B-D). We observed
181 that not all vDNAs were associated to a transcriptional focus, most likely because of
182 the presence of silent episomal forms. On the other hand, an abundant part of vRNA
183 foci colocalized with vDNA (Fig. 2B and C), meaning that we are able to detect single
184 transcribing proviruses. Taken together, our results suggest that we are able to track
185 down transcribing proviruses in the nuclear space of different cells and distinguish
186 them from silent forms.

187 **Nuclear localization of actively transcribing proviruses at single-cell level in** 188 **dividing and non-dividing cells.**

189 The location of actively transcribing proviruses in the nuclear space of dividing cells is
190 still a subject of debate (Achuthan et al., 2018; Burdick et al., 2017; Chin et al., 2015;
191 Di Primio et al., 2013; Lelek et al., 2015; Marini et al., 2015), whereas their nuclear
192 location in terminally differentiated cells, as far as we know, has never been studied
193 before. In dividing cells, the 3D analysis of the nuclear location of the vDNA showed
194 the vDNA signals at 48 h p.i. to be more randomly distributed throughout the nucleus
195 compared to the vDNA spots at seven days p.i. (avg distances from the nuclear
196 envelope (NE): ~2.5 μm at 48 h p.i. vs ~1.4 μm at 7 days p.i.) (Fig. 3A). The difference
197 in the average distance of the vDNA spots from the NE between the early and late time
198 points p.i. may be due to the co-existence of heterogeneous viral forms at 48 h p.i.
199 (episomal and proviral forms), whereas the vDNA population is more homogeneous at
200 seven days p.i. (Fig. 1D, Fig. 3A). The episomal forms are distributed at a slightly
201 greater distance from the NE than the mixed vDNAs population at 48 hour p.i. when
202 compared to the vDNA at 7 d p.i. (Fig. 3A). Interestingly, we did not detect differences
203 between the distances of the vRNA foci from the NE at both time points (48h p.i. and

204 7d p.i.) and the vDNA spots at seven days p.i. ($< 2 \mu\text{m}$ in avg), indicating that in dividing
205 cells the integration of the proviral DNA occurs early during infection near to the NE
206 (Fig. 3A). We performed similar 3D analysis to calculate the distances of vDNAs and
207 vRNAs from the NE in non-dividing cells at three days p.i.. The lack of mitosis hinders
208 the loss of the episomal forms in non-dividing cells (Fig. 3B). However, when we
209 compared the integration-defective viruses (only episomal forms) with the integration-
210 efficient viruses (episomal and proviral forms), the vDNAs of the latter were found
211 slightly closer to the NE (Fig. 3B). While the vRNAs (viral transcription foci) were closer
212 to the NE with respect to episomal forms ($\sim 2.5 \mu\text{m}$ for the vDNA IN_{D116A} vs $\sim 1.8 \mu\text{m}$ for
213 the vRNA) (Fig.3B). Finally, our data show a similar nuclear spatial distance of viral
214 transcriptional foci from the NE at single-cell level in both dividing and non-dividing
215 cells ($\sim 1.8 \mu\text{m}$ in HeLa cells and in THP-1 cells) (Fig.3C).

216 **Late reverse transcribed DNAs separate from IN proteins sequestered in CPSF6** 217 **clusters.**

218 A long-standing question in the early steps of HIV life cycle is related to the study of
219 IN-vDNA dynamics after nuclear entry. How long does the association last and can we
220 detect it? There are, indeed, multiple difficulties due to the likely short-time nature of
221 the event or due to the technical limitations of vDNA and IN visualization. Therefore,
222 we exploited our vDNA tracking system to investigate about IN proteins localization in
223 primary CD4⁺T cell and THP-1 cells, challenging both cell types with HIV-1 ANCH3.
224 We found in both cell types that the vDNA/IN association event was very rare (Fig. 4A).
225 Nuclear IN proteins were found in the nucleus separated from the late reverse
226 transcripts (Fig. 4A). To confirm our data we performed live-imaging, asking whether
227 we could pinpoint the dynamic evolution of vDNA/IN association in the nucleus of
228 infected cells by coupling the HIV-1 ANCHOR system with the GIR virus (generous gift
229 from Edward Campbell) (Dharan et al., 2016; Hulme et al., 2015). GIR virus is
230 produced using a viral genome carrying the IN mutated in the catalytic site (HIV-1
231 ANCH3 IN_{D116A}) together with Gag-integrase-Ruby (GIR) plasmid. As consequence,
232 the only active IN in these viral particles is the IN-Ruby (Fig. 4B, Fig. S3). During a time
233 lapse of 4 hours in HeLa cells (Fig. S3), we have observed the signals of the IN and of
234 the vDNA always separated (~ 0.6 to $0.8 \mu\text{m}$) (Fig. S3, video 5) corroborating the
235 results in fixed cells (Fig. 4A). Importantly, we did not synchronize the infection to have
236 the opportunity to visualize in a single cell different viral dynamics. We found several

237 IN foci alone and then colocalizing with the vDNA before the separation (Fig. 4B, movie
238 6, 7). We analysed the association of the two signals that rapidly (~10 min) separated
239 (Fig. 4B, video 6,7). These data suggest that the IN proteins that are part of the mature
240 PIC cannot be detected by a conventional light microscopy. Next, we investigated
241 whether the viral IN proteins are retained in particular nuclear regions by some nuclear
242 host factors. We found that the viral IN occupies, in nearly all cases analyzed, the same
243 positions of the host Cleavage and Polyadenylation Specificity Factor subunit 6
244 (CPSF6), in both dividing and non-dividing cells (IN to CPSF6 ~ 94.4% in CD4+T cells
245 and ~92.5% in THP-1 cells) (Figure 4C). Of note, HIV-1 reprograms the nuclear
246 localization of CPSF6 from being randomly dispersed in the nucleoplasm to form
247 particular aggregates in both primary lymphocytes and macrophages (Fig. 4C). Taken
248 together our results indicate that IN proteins after viral nuclear entry are retained in
249 CPSF6 clusters, while the late reverse transcribed DNA separates from these sites
250 (Fig. 4A-C). We next wondered if other viral components are also hosted in CPSF6
251 MLOs together with the IN. Adapting our RNA FISH protocol with a longer probe
252 hybridization and coupling it with the immunostaining of CPSF6 (Immuno-RNA FISH)
253 (Fig. S4), we uncovered the presence of incoming vRNA inside the MLOs (Fig. 4D).
254 Upon NEV treatment, HIV-1 genomes locate in CPSF6 clusters, both in CD4+T and
255 THP-1 cells. In physiological conditions it seems that vRNA/CPSF6 association events
256 are more abundant in non-dividing cells than in dividing cells (~87% vs. ~33%), at 2
257 days post infection (Fig. 4D). Overall, the sequestration of viral IN proteins and viral
258 genomes in CPSF6 clusters hints that CPSF6 MLOs could serve as sites to release a
259 mature PIC that contains only few IN proteins needed for the integration step
260 (Ballandras-Colas et al., 2017; Hare et al., 2009). We called these particular nuclear
261 niches HIV-induced membraneless organelles (HIV-1 MLOs).

262 **HIV-induced membraneless organelles (HIV-1 MLOs) are sites of nuclear reverse** 263 **transcription.**

264 To better characterize the role of HIV-1 MLOs, we performed Immuno-RNA FISH at
265 different time post infection in THP-1 cells. We observed the majority of vRNAs
266 retained in CPSF6 clusters at 2 days p.i., while at 3 days p.i. and even more at 7 days
267 p.i. almost half of the total vRNA foci were excluded from CPSF6 clusters (Figure 5A).
268 Genomic vRNAs localize 100% with CPSF6 upon NEV treatment at all times p.i. (Fig.
269 5A), this suggests that the vRNA transcription foci locate outside CPSF6 clusters. What

270 is the functional meaning of the incoming vRNA sequestration in CPSF6 clusters? To
271 answer to this question we performed Chromatin Immunoprecipitation (ChIP) of the
272 endogenous CPSF6 protein in infected and uninfected THP-1 cells at 2 days p.i.,
273 followed by real-time PCR (Fig. 5B). Early, intermediate and late RT products were
274 amplified using appropriate primers. Of note, early transcripts were more abundant
275 than others, revealing an “ongoing” reverse transcription inside CPSF6 clusters. (Fig.
276 5B). Our results explain previous data showing EdU-labeled viral episomal forms
277 clustering in nuclear niches of macrophages (Francis et al., 2020; Rensen et al., 2020).
278 Importantly, the presence of the IN inside HIV-1 MLO is independent of the presence
279 of the reverse transcription, highlighting that the retrotranscribed DNA is not the driving
280 force of the HIV-1 MLOs formation (Fig 5C). Since CPSF6 participates to the viral
281 nuclear translocation and post-nuclear entry steps by interacting with the viral CA
282 (Bejarano et al., 2019; Burdick et al., 2017; Lee et al., 2010; Price et al., 2014) (Francis
283 et al., 2020), it might be that the viruses inside HIV-1 MLOs have not yet completed
284 the uncoating process.

285 **The integration of the transcriptionally active proviruses occurs outside HIV-1** 286 **MLOs.**

287 CPSF6 phase separation does not randomly occur in the nuclear space. CPSF6
288 clusters fully colocalize with the marker of nuclear speckles (NSs), SC35 (Fig. 6 A-C).
289 Importantly, we remarked that CPSF6 and SC35 signals mainly occupy the
290 interchromatin space (Fig. 6A). NSs are, indeed, interchromatin granules (Spector and
291 Lamond, 2011). SC35 strongly associates to another speckle factor, SON,
292 independently of viral infection (Pearson’s $r \sim 0.995$), indicating that CPSF6 clusters in
293 the host NS (Fig. 6B). Contrary to EdU labeling (Rensen et al., 2020), the HIV-1
294 ANCHOR system allows the visualization of a single provirus (Fig.1C) and does not
295 interfere with viral transcription (Blanco-Rodriguez et al., 2020). Thus, we asked where
296 in the nuclear space the viral expression takes place. We first observed that 3 days p.i.
297 almost all late reverse transcripts are excluded from CPSF6 clusters (Fig.6B), as
298 expected from the vDNA/IN separation data (Fig. 4A and B). We computed, as well,
299 the distances of the vDNAs from the boundary of the closest NS (avg $\sim 0.6 \mu\text{m}$) (Fig.
300 6B). Similar data were obtained upon integration inhibition (+RAL), where the majority
301 of episomal DNA forms locate outside CSPF6 clusters and in average $\sim 0.4 \mu\text{m}$ from
302 SC35 (Fig. S5A). Taking into account that we found the late reverse transcribed DNA

303 located outside HIV-1 MLO, to understand the exact location of transcriptionally active
304 proviruses we used MCP-MS2 RNA labelling system. We observed that MCP-GFP is
305 unable to label the viral incoming RNA (Fig.6C). Under NEV treatment, MCP-GFP is
306 filtered out of HIV-1 MLOs as shown by the intensity profiles, whether in physiological
307 conditions it labels the viral transcription foci (Fig. 6C). Active proviruses are excluded
308 from CPSF6 clusters (Fig. 6D) and located in average at a distance from the closest
309 CS35 NS $\sim 0.6 \mu\text{m}$). These results are independent of the presence of vpx (Fig. S5B)
310 that we used to increase viral infectivity in THP-1 cells (Hrecka et al., 2011; Laguette
311 et al., 2011). Taken together, we display that both vDNA (episomal and proviral forms)
312 and vRNA foci (active proviruses) are excluded from HIV-1 MLOs (Fig. 6E), clearly
313 indicating that these structures cannot be sites for viral integration or replication. More
314 in detail, we found foci of viral transcription located in avg at a distance $\sim 0.9 \mu\text{m}$ from
315 the closest HIV-1 MLO (CPSF6+SC35), while total vDNAs were found $\sim 1.8 \mu\text{m}$ from
316 the nearest HIV-1 MLO (Fig. 6F). These data were corroborated by another vRNA
317 labelling approach, immuno-RNA FISH, coupled to HIV-1 ANCHOR to detect the
318 transcribing proviruses, indicating that viral integration and transcription occur outside
319 CPSF6 clusters (Fig. 6G). Of note, we confirmed the results obtained in THP-1 cells
320 (Fig. 5A) in primary monocyte-derived macrophages (MDMs), using an HIV-1 GFP
321 reporter virus (Fig. 7). Also in the MDMs we could appreciate the blockade of the
322 incoming vRNA in CPSF6, while the transcription foci locate outside these organelles
323 (Fig. 7). Finally, we were able to correlate the percentage of vRNA foci that locate
324 outside the MLOs per nucleus and the viral GFP expression (Pearson's $r \sim 0.63$),
325 showing that those are integration and transcription sites of HIV-1 (Fig.7).

326

327 **HIV-1 integration sites are marked by LEDGF.**

328 We extended our study on THP-1 cells at 3 days p.i. to investigate whether Lens
329 Epithelium-Derived Growth Factor (LEDGF), which is a partner of the viral IN and a
330 HIV-1 integration sites selection factor (Cherepanov et al., 2003; Ciuffi et al., 2005;
331 Emiliani et al., 2005; Ferris et al., 2010; Hare et al., 2009; Lelek et al., 2015; Llano et
332 al., 2006; Shun et al., 2008; Shun et al., 2007; Wang et al., 2014), is associated to the
333 proviruses forming a complex visible by imaging. We observed that CPSF6 proteins
334 cluster in proximity of LEDGF sites ($\sim 43\%$), without co-localizing (Fig. 8A). There is a
335 similar number of LEDGF clusters in both infected and uninfected cells (Fig. 8A), while
336 CPSF6 clusters are mainly formed upon infection, suggesting that CSPF6 is prompted

337 by the virus to localize near the pre-existing LEDGF regions (Fig.8A). Of note, the
338 PWWP domain of LEDGF has been shown to interact with H3K36me3 (Pradeepa et
339 al., 2014; Pradeepa et al., 2012), which is a marker of euchromatin. In particular, this
340 post-translational modification is enriched in HIV-1 integration sites (Ciuffi et al., 2005;
341 Lelek et al., 2015; Vansant et al., 2020; Wang et al., 2009). Therefore, we analysed
342 the location of proviral foci of transcription in relation to LEDGF. In average ~64%
343 vDNA and ~73% vRNA foci per nucleus were found in complex with LEDGF (Fig. 8B).
344 Importantly, LEDGF is also known to interact with splicing factors (Singh et al., 2015).
345 This is in agreement with our data showing vDNA and vRNA localized in avg ~ 0.6 μ m
346 from the closest NS (Fig. 6B and D). Next we have characterized in more detail the
347 viral genome associations with LEDGF with respect to CPSF6. We calculated that ~
348 87.9% of the vDNA/LEDGF complexes and ~80% of vRNA foci/LEDGF complexes are
349 uncoupled to CPSF6 (Figure 8B). We found only few vDNA (~12.1%) and vRNA
350 (~20%) foci associated to LEDGF clusters near to CPSF6 (Fig. 8B). Our results
351 suggest that the two cellular factors, CPSF6 and LEDGF, orchestrate two sequential
352 steps of viral replication, the maturation of the PIC and its integration, respectively (Fig.
353 9). Functional proviruses are not located inside HIV-1 MLOs, but in external active
354 chromatin domains, enriched in LEDGF (Fig. 8B) and in proximity of SC35 NS (Fig.
355 6D), likely to benefit of a favorable environment for viral replication.

356

357 **Discussion**

366 Studies of parasites that permanently integrate into the host genome show that they
367 have evolved to target chromatin in such a way as to optimize their coexistence with
368 the host and favor the release of new viral progeny (Bushman, 2003; Craig and
369 Marszalek, 2002). HIV-1 needs to rapidly release high levels of newly generated
370 viruses after infection, intuitively explaining the preference of active genes as
371 integration targets (Ciuffi et al., 2005; Di Nunzio et al., 2013; Lelek et al., 2015;
372 Maldarelli, 2016; Schroder et al., 2002). However, the nuclear location of actively
373 transcribing individual proviruses in dividing or non-dividing cells has never been
374 visualized before. Thus far, the direct detection of HIV-1 genomes after reverse
375 transcription and the distribution of proviral transcriptional foci has been technically
376 challenging. HIV-1 ANCHOR system allows the live tracking of different nuclear late
377 retrotranscribed DNA forms (Fig.1A-C). We observed a homogenous population

378 formed by proviral DNA with low diffusion coefficient. Episomal forms showed a
379 heterogeneous behavior, characterized by two different populations, implying that
380 these two viral forms can interact with different factors in the nuclear space (Fig. 1D).
381 Moreover, imaging analysis showed that viral episomal forms identified by the
382 accumulation of OR-GFP on ANCH3 sequences gave rise to brighter signals than
383 proviral forms in HeLa cells (Fig. 2A). This phenomenon could explain the differences
384 in behavior between integrated and non-integrated forms (Fig.1D). Intriguingly, we
385 found that episomal vDNAs form clusters, which could result in a brighter signal than
386 integrated forms (Fig. S2C, video 4). Next, to track the nuclear location of functional
387 proviruses, we co-labeled vDNA and vRNA by combining HIV-1 ANCHOR technology
388 with RNA FISH or with MCP-MS2 system (Tantale et al., 2016) in the main target cells
389 of HIV-1 (Fig.2A-D, Fig.S2A and B). Therefore, we investigated the spatial location of
390 proviruses in dividing and non-dividing cells. Three-dimensional analysis of the
391 distribution of vDNAs during early (48 h p.i.) infection in mitotic cells displays that they
392 are more randomly distributed than the proviral DNA from cells at 7days p.i. (Fig. 3A).
393 We also observed that the location of viral transcription sites (vRNA) is highly similar
394 between early and late time points of infection, indicating that in HeLa cells the proviral
395 DNAs, the only transcribing forms (Fig. 2A), immediately localize to near the NE early
396 after infection (Fig. 3A). This vicinity to the NE was detected as well in non-dividing
397 cells (Fig. 3B), highlighting that in both mitotic and non-mitotic cells the proviruses
398 locate in the nuclear periphery (Fig.3C). We next investigated the interplay among viral
399 components and their association with host factors during post-nuclear entry steps. IN
400 proteins strongly co-localize with CPSF6 clusters in macrophage-like cells and in CD4⁺
401 T lymphocytes at early time of infection (Fig. 4C), in agreement with another study
402 (Francis et al., 2020). Contrary to CPSF6, the late vDNA products of retrotranscription
403 rarely co-localize with IN in both types of cells (Fig. 4A). However, in live imaging we
404 pinpointed the budding of newly synthesized late reverse transcribed DNA from the IN
405 clusters, which occurs within minutes (Fig.4B, video 6,7). These results are in line with
406 the dynamic coexistence of the IN and vDNA, which remain separated but in the
407 proximity for several hours, as it has been shown by real-time imaging in HeLa cells
408 (Fig. S3, Table S1, Table S2, video 5). This result can appear in contrast with recent
409 data from other groups and from us obtained with another DNA labeling technology,
410 EdU (Francis et al., 2020; Rensen et al., 2020), showing the vDNA and the IN strongly
411 colocalized with CPSF6. This apparent discrepancy can be explained by the intrinsic

412 features of vDNA labeling tools. While EdU labeling cannot provide direct information
413 on viral replication, as EdU reduces viral transcription (Rensen et al., 2020), HIV-1
414 ANCHOR system allows the detection of late reverse transcripts (Fig.1A) that can
415 generate functional proviral DNA, as we observed in HeLa cells, human lymphocytes,
416 and macrophages (Fig. 2A-D). Thus, we asked whether CPSF6 clusters are
417 physiological sites of nuclear RT and of viral replication. First, we performed ChIP of
418 the endogenous CPSF6 followed by real time PCR in THP-1 cells infected or
419 uninfected (48 h p.i.). The PCR results show an abundance of early and intermediate
420 RT products in comparison to late RT products, indicating an ongoing RT process in
421 CPSF6 sites. These results are in agreement with a detection of the nascent vDNA
422 (Fig. 4B) and with the labeling of the vDNA in these sites (Rensen et al., 2020). Second,
423 we were able to correlate the progression of the viral infection with the nuclear location
424 of the vRNA foci (Fig. 5A). At early time p.i. almost all vRNA are sequestered in CPSF6
425 clusters to be reverse transcribed (Fig.5A). Concurrently with the advancement of the
426 viral infection we observed an increase in vRNA foci outside CPSF6 clusters, these
427 foci are never present in cells treated with NEV where the viral replication is completely
428 blocked (Fig. 5A). Importantly, our results show a positive correlation between the
429 number of vRNA foci excluded from CPSF6 clusters and the GFP expression (HIV-1
430 reporter gene) (Fig. 7). Thus, HIV-1 induces the formation of novel membraneless
431 organelles (MLOs) retaining CPSF6 proteins and viral components, such as IN and
432 viral RNA genomes to host viral reverse transcription (Fig. 4C and D, 5A and B). HIV-
433 1 MLOs form in the interchromatin space, remodeling the host nuclear speckles,
434 characterized by the presence of SC35 and SON (Fig.6A and B). Likely, CPSF6
435 relocates to speckles prompted by the virus to usurp functions linked to these MLOs.
436 We show that the formation of CPSF6 cluster is independent of viral DNA integration
437 or viral DNA synthesis (Fig. S5A, Fig. 5C) and that late reverse transcribed products
438 are mainly excluded from them (Fig. 6B and E, Fig.7). These results are in agreement
439 with a rapid exclusion of late retrotranscribed DNAs from the IN proteins that are
440 retained in CPSF6 clusters (Fig. 4A-C). Next, we calculated the distribution of the
441 actively transcribing proviruses in the nuclear landscape. Interestingly, we observed
442 that the MCP-MS2 system detects only the vRNA associated with viral replication sites,
443 as MCP-GFP is unable to penetrate HIV-1 MLOs that shield the incoming vRNA
444 genome, acting as selective filters (Fig. 6C). When we compared the distances from
445 the boundary of the closest HIV-1 MLOs (CPSF6 + SC35), we observed that the vRNA

446 transcription foci were closer than the vDNAs, indicating that the HIV-1 MLOs-
447 neighbouring regions are the hub of viral replication (Fig. 6 F-G). We also observed
448 that CPSF6 relocates to the vicinity of LEDGF during HIV infection (Fig. 8A). LEDGF
449 associates to highly-spliced transcriptional units through its direct interaction with
450 several splicing factors (Singh et al., 2015) and determines HIV-1 integration sites
451 distribution in active chromatin sites (Ciuffi et al., 2005; Ferris et al., 2010; Shun et al.,
452 2007). However, the visualization of a complex formed by the transcribing provirus and
453 LEDGF remained utopian for a long time. Here, we were able to visualize by
454 fluorescence microscopy a complex formed by the vDNA or vRNA and LEDGF. Almost
455 80% of those complexes are formed by LEDGF uncoupled to CPSF6 (Fig. 8B).
456 Nonetheless, we observed that less than 20% of them can include CPSF6 associated
457 to LEDGF. Whether there is a functional difference between these two complexes it
458 can be further investigated in future studies. Overall, our study highlights the proviral
459 location in the nuclear landscape remodelled by the viral infection (Fig. 9). We found
460 that HIV-1-MLOs sequester the viral IN (Fig. 4C, Fig.5C), as well viral RNA genomes
461 (Fig. 5A) and rapidly release the late retrotranscribed DNA, acting as HIV-1 reverse
462 transcription and PIC maturation sites (Fig.4B, Fig. 5A and B). Thus, HIV-1 MLOs play
463 a role prior to the integration step. Taken together our results show that functional
464 proviruses establish near to the NE (Fig. 3C), excluded from CPSF6 clusters, but
465 locate in a favorable transcriptional environment (Fig. 6D, Fig.8B) at less than 1 μ m
466 from HIV-1 MLOs (Fig.6F). Our study supports how new single-cell level approaches
467 are pivotal in the study of functional viral nuclear dynamics (Fig.9), to discriminate the
468 cells susceptible to fuel viremia or that concur to viral persistence.

469

470 **Materials and Methods**

471 **Cell lines, primary cells and generation of genetically modified single-cell** 472 **clones.**

473 HEK 293T cells (ATCC) are human embryonic kidney cells used to produce lentiviral
474 vectors and HIV-1. HeLa P4R5 reporter cells (Charneau et al., 1994). HeLa MCP-GFP
475 is a HeLa clone stably expressing MCP-GFP bacterial fusion protein (kind gift from E.
476 Bertrand) (Tantale et al., 2016). Jurkat cells (ATCC) are human immortalized T
477 lymphocytes derived from acute T cells leukemia. THP-1 cells (ATCC) are human

478 immortalized monocyte cells derived from acute monocytic leukemia, which, once
479 seeded, were differentiated into macrophage-like cells under Phorbol 12-myristate 13-
480 acetate (PMA) treatment (167nM). SupT1R5 cells are T lymphoblastic lymphoma cells
481 which were transduced to stably express CCR5 (kind gift of N. Casartelli). HEK293T
482 cells and HeLa cells were cultivated in DMEM medium supplemented with 10% Fetal
483 Bovine Serum (FBS) and 1% penicillin-streptomycin. Jurkat, SupT1R5 and THP-1 cells
484 were cultivated in RPMI 1640 medium supplemented with 10% Fetal Bovine Serum
485 (FBS) and 1% penicillin-streptomycin solution. Primary CD4⁺T and MDM cells were
486 purified from healthy donors' blood obtained via EFS (Etablissement Français du Sang,
487 Paris), through density gradient centrifugation with Ficoll 400 and isolation of PBMCs
488 buffy coat. CD4⁺T cells positive selection was performed with human CD4 Microbeads
489 (Miltenyi Biotec #130-045-101). The day after CD4⁺T cells were activated with T cell
490 Activation/Expansion kit (Miltenyi Biotec #130-091-441) according to the datasheet,
491 complete RPMI 1640 medium was supplemented with interleukin-2 (IL-2) (400
492 IU/mL). For MDMs the PBMCs were incubated at 37°C for 2 hours, then, non-adherent
493 cells were washed away and complete RPMI 1640 medium was supplemented with
494 M-CSF (10 ng/mL). After 3 days, the medium was changed with RPMI without M-CSF
495 and cells were left to differentiate for other 4 days before proceeding with infection.
496 HIV-1 ANCH3 single-cell clone was generated starting from HeLa P4R5 cells which
497 were infected with HIV-1 ANCH3 virus at MOI 1. Cells were diluted to 1 cell per well,
498 in 96-well plates. Cell-clone colonies were tested for β -galactosidase expression to
499 check viral expression (kit Roche #11758241001). Positive clones were transduced
500 with lentiviral vector (LV) CMV-OR-GFP for imaging analyses of HIV-1 ANCH3
501 provirus. All cells were kept in incubator at 37°C and 5% CO₂.

502

503 **Plasmids, lentiviral vectors and viral productions**

504 HIV-1 Δ EnvIN_{HA} Δ Nef plasmid encodes for the Δ EnvHIV-1 LAI (BRU) viral genome
505 where the Integrase (IN) protein is fused to the hemagglutinin (HA) tag (kindly provided
506 by F. Mammano)(Petit et al., 1999; Petit et al., 2000). HIV-1 Δ EnvIN_{HA} Δ Nef ANCH3
507 (HIV-1 ANCH3) was obtained through ANCH3 insertion: ANCH3 sequence was cloned
508 by PCR using the template plasmid pANCH3 as we previously described in Blanco et
509 al. (Blanco-Rodriguez et al., 2020). The ANCHOR™ technology and sequences are
510 exclusive property of NeoVirTech (Germier et al., 2017; Mariame et al., 2018). HIV-

511 1ΔEnv IN_{HA}(D116A) ΔNef ANCH3 was obtained by insertional mutagenesis using the
512 QuikChange II XL Site-Directed Mutagenesis kit (Agilent #200522), for integrase (IN)
513 mutation at D116. The lentiviral vector plasmids CMV OR-GFP and CMV OR-
514 SANTAKA were obtained by cloning OR-GFP/OR-SANTAKA (plasmids from
515 NeoVirTech) in a pTripCMV (ΔU3) plasmid through PCR and cloned using restriction
516 site, AgeI and SgrDI. HIV-1ΔEnvIN_{HA}ΔNef ANCH3 MS2 plasmid was obtained by
517 inserting the MS2x64 sequence amplified by PCR from pMK123-MS2x64 (Tantale et
518 al., 2016) in HIV-1ΔEnvIN_{HA}ΔNef ANCH3. Lentiviral vectors and HIV-1 viruses were
519 produced by transient transfection of HEK293T cells through calcium chloride
520 coprecipitation. Co-transfection was performed as following, LV carrying OR-GFP/OR-
521 SANTAKA: 10 μg of OR-GFP/OR-SANTAKA LV, 10 μg of NDK plasmid (gag-pol-tat-
522 rev) and 2.5 μg of pHCMV-VSV-G envelope expression plasmid; LV carrying MCP-
523 GFP (kindly provided by E. Bertand): 10 μg of MCP-GFP, 10 μg of NDK plasmid (gag-
524 pol-tat-rev) and 2.5 μg of pHCMV-VSV-G envelope expression plasmid; HIV-1ΔEnv
525 pseudotyped with VSV-G: 10 μg HIV-1ΔEnvIN_{HA}ΔNef (IN WT or IN(D116A)) plasmid
526 and 2.5 μg of pHCMV-VSV-G plasmid. VSV-G/HIV-1ΔEnv IN_{HA}(D116A) ΔNef ANCH3
527 has been also produced in combination with GIR (Gag-IN-Ruby plasmid, kindly
528 provided by E. Campbell) (Dharan et al., 2016; Hulme et al., 2015). For THP-1
529 infection, HIV-1 ANCH3 or HIV-1 ANCH3 MS2 viruses and LV OR-GFP or LV MCP-
530 GFP were all produced adding 3 μg of SIV_{MAC} Vpx (Durand et al., 2013) at the moment
531 of HEK293T transfection. MDMs were infected with a virus HIV-1 ΔEnv Δnef GFP
532 complemented with Vpx (Rensen et al., 2021). After the collection of the supernatant
533 48h post-transfection, lentiviral particles were concentrated by ultracentrifugation for 1
534 h at 22000 rpm at 4°C and stored at -80°C. Lentiviral vectors and viruses were tittered
535 through late reverse transcripts (LTR) qPCR in HEK293T cells.

536

537 **Quantitative PCR and primers**

538 Total DNA of 10⁶ infected cells was extracted at 6 hours post infection for Late Reverse
539 Transcripts (LRTs) qPCR and 24 hours post infection for 2LTR-circles and ALU-PCR,
540 through QIAmp DNA micro kit (QIAGEN #56304). Real-Time PCR of LRTs was
541 performed to assess DNA synthesis and used to normalize qPCR data on viral input,
542 the reactions were carried on in 20 μL, in iTaqUniversal SYBR Green Supermix (Bio-
543 Rad #1725124) using primers for U3 sequence: U3 FX: 5'-
544 TTCCGCTGGGGACTTTCCAGGG-3', U3 RX: 5'-AGGCTCAGATCTGGTCTAACC-3'.

545 Real-Time PCR of 2LTR-circles was used to assess nuclear import efficiency.
546 Reactions were performed in 20 μ L, in Maxima Probe/ROX qPCR Mastermix
547 (ThermoFisher #K0232) using primers for 2LTR-circle junction: 2LTR FX: 5'-
548 AACTAGGGAACCCACTGCTTAAG-3', 2LTR RX: 5'-
549 TCCACAGATCAAGGATATCTTGTC-3', 2-LTR probe: 5'-(FAM)-
550 ACACTACTTGAAGCACTCAAG-GCAAGCTTT-(TAMRA)-3'. Real-Time PCR of
551 proviral integrations consisting in a first non-kinetic PCR in 50 μ L in Platinum SuperFi
552 DNA Polymerase (ThermoFisher #12351250) and in a second step of qPCR reaction
553 in 20 μ L in Maxima Probe/ROX qPCR Mastermix (ThermoFisher #K0232). Primer Alu
554 166: 5'-TCCCAGCTACTCGGGAGGCTGAGG-3', Alu 2: 5'-
555 GCCTCCCAAAGTGCTGGGATTACAG-3', LambdaU3: 5'-
556 ATGCCACGTAAGCGAAACTTTCCGCTGGGGACTTTCCAGGG-3' for ALU PCR;
557 Lambda: 5'-ATGCCACGTAAGCGAAACT-3', U5: 5'-CTGACTAAAAGGGTCTGAGG-
558 3', Probe: 5'-(FAM)- TTAAGCCTCAATAAAGCTTGCCTTGAGTGC-(TAMRA) for ALU
559 qPCR (Di Nunzio et al., 2013). In all experiments β -actin detection was used for
560 normalization. β -actin FX: 5'-AACACCCCAGCCATGTACGT-3', β -actin RX: 5-
561 CGGTGAGGATCTTCATGAGGTAGT-3', β -actin probe: (FAM)-
562 CCAGCCAGGTCCAGACGCAGGA-(BHQ1).

563

564 **Epifluorescence and Immunofluorescence of HIV-1 infected cells**

565 For imaging studies in adherent cell-lines, the cells were plated on coverslips (12mm
566 diameter in 24 well plates or 18 mm diameter in 12 well plate, #1, ThermoFisher) at
567 least 24h before fixation. For HIV-1 ANCH3 imaging, HeLa P4R5 cells were
568 transduced with OR-GFP LV (MOI 0.2) and then infected usually 24 hours later with
569 HIV-1 ANCH3 or HIV-1 IN_{D116A} ANCH3 at different MOIs (from 5 to 30). NEVIRAPINE
570 (NEV) 10 μ M or RALTEGRAVIR (RAL) 20 μ M were used to block respectively DNA
571 synthesis or integration. All THP-1 cells studies were carried on after 48h of
572 differentiation with PMA (167 nM), then, they were transduced with LV OR-GFP Vpx
573 (MOI 0.5) or LV MCP-GFP Vpx (MOI 2) and 48 h later they were infected with HIV-1
574 ANCH3 Vpx (MOI 10-20) or HIV-1 ANCH3 MS2 \pm Vpx (MOI 2.5). The medium was
575 always supplemented with PMA. For HIV-1 ANCH3 imaging in primary lymphocytes,
576 CD4⁺T cells, 3 days after activation, were transduced with OR-GFP LV (MOI 0.5) then
577 infected with HIV-1 ANCH3 (MOI 100). The day of fixation cells in suspension were

578 seeded on poly-L-lysine (Sigma #P4707) coated coverslips and shortly centrifuged to
579 allow attachment. The day of fixation all cells were washed with PBS and fixed with
580 4% PFA for 15 minutes. For protein staining, cells were treated with glycine 0.15% for
581 10 min, permeabilized with 0.5% Triton X-100 for 30 min and blocked with 1% bovine
582 serum albumin (BSA) for 30 min. All incubations were carried out at room temperature,
583 in the dark, in humid chamber, 1h with primary antibodies and 45 min with secondary
584 antibodies. Washes between antibody incubations and antibodies dilution were done
585 in 1% BSA. Primary antibodies were diluted as follows: anti-HA 1:500 (Roche
586 #11867423001), anti-HIV-1 p24 (CA) 1:400 (NIH #3537), anti-CPSF6 1:400 (Novus
587 Biologicals #NBP1-85676), anti-SC35 1:200 (Abcam #ab11826), anti-LEDGF 1:200
588 (BD Bioscience #611715). Secondary antibodies used were the following: Goat anti-
589 Mouse Alexa-647 1:300 (1:100 for CA) (Invitrogen #A21235); Donkey anti-Rat Alexa-
590 488 1:100 (Invitrogen# A21208) for IN-HA or Goat anti-Rat Alexa-647 1:300 (Invitrogen
591 #A21247), 1:100 for IN-HA; Donkey anti-Rabbit Cy3 1:500 (Jackson Lab #711-165-
592 152). Finally, cells were stained with Hoechst 33342 1:5000 (Invitrogen #H3570) for 5
593 minutes. Coverslips were mounted on glass slides (Star Frost) with Prolong Diamond
594 Antifade Mountant (Life Technologies #P36970). Confocal microscopy was carried out
595 with a Zeiss LSM700 inverted microscope, with a 63X objective (Plan Apochromat, oil
596 immersion, NA=1.4).

597

598 **RNA FISH**

599 For RNA FISH studies in adherent cell-lines, the cells were seeded on coverslips. HeLa
600 P4R5 cells expressing OR-GFP were infected with HIV-1 ANCH3 (MOI 30) with or
601 without RAL (20 μ M) or infected with HIV-1 ANCH3 (MOI 5). Jurkat cells expressing
602 OR-GFP were infected with HIV-1 ANCH3 (MOI 5). Primary activated CD4⁺T cells, 3
603 days after activation, were together transduced with OR-GFP LV (MOI 10) and infected
604 with HIV-1 ANCH3 (MOI 50). THP-1 cells were differentiated with PMA for 48h and,
605 after 48h transduction with LV OR-GFP Vpx (MOI 0.5), the cells were infected with
606 HIV-1 ANCH3 Vpx (MOI 20). Primary MDMs were seeded before differentiation on
607 coverslips, and after 7 days, transduced with LV OR-GFP Vpx (MOI 10) and infected
608 with HIV-1 ANCH3 Vpx (MOI 40). The day of fixation suspension cells were seeded on
609 poly-L-lysine (Sigma #P4707) coated coverslips and centrifuged to allow attachment.
610 Then, cells were washed with PBS and fixed with 4% PFA for 15 minutes and

611 incubated in 70% ethanol at -20°C at least for one night. Primary smiFISH probes have
612 been designed against HIV-1 *pol* transcript and a shared readout sequence for
613 secondary probe alignment. Twenty-four smiFISH probes (Table S3) against HIV *pol*
614 were designed with Oligostan (Tsanov et al., 2016) and purchased from Integrated
615 DNA Technologies (IDT). Primary probes were pre-hybridized with a secondary FLAP
616 probe conjugated to Cy5 fluorophore through pairing with the readout sequence
617 (Eurofins). Washes and hybridization were performed with Stellaris Buffers (WASH
618 buffer A, WASH buffer B, Hybridization Buffer; LGC Biosearch Technologies),
619 following the manufacturer protocol. Hybridization with the probe was carried out at
620 37°C in a dark humid chamber for 5 hours. Finally, cells were stained with Hoechst
621 33342 1:5000 (Invitrogen #H3570) for 5 minutes. Coverslips were mounted on glass
622 slides (Star Frost) with Prolong Diamond Antifade Mountant (Life Technologies
623 #P36970). Confocal microscopy was carried out with a Zeiss inverted LSM700
624 microscope, with a 63X objective (Plan Apochromat, oil immersion, NA=1.4).

625 **IMMUNO-RNA FISH**

626 THP-1 and primary MDM cells were seeded on coverslips and infected with HIV-1
627 ANCH3 vpx (MOI 20). SupT1R5 cells were infected with HIV-1 ANCH3 (MOI 20) and
628 the day of fixation they were seeded on poly-L-lysine (Sigma #P4707) coated
629 coverslips and centrifuged to allow attachment. The day of fixation the coverslips with
630 the cells were washed with PBS and fixed with 4% PFA for 15 minutes to proceed with
631 CPSF6 immunostaining. Coverslips were incubated with a blocking/permeabilization
632 solution (PBS-BSA 1%, Vanadyl ribonucleoside complexes (VRCs) solution 2mM
633 (Sigma #94742), TRITON-X 0.3%) for 1 h. Then, the coverslips were incubated with
634 anti-CPSF6 1:400 (#NBP1-85676) in blocking/permeabilization solution for 1h, washed
635 and incubated for 45 min with anti-Rabbit secondary antibody, at room temperature, in
636 the dark, in humid chamber. The coverslips were fixed again in PFA 4% for 10 min.
637 Subsequent RNA FISH and mounting protocol was carried out as mentioned in the
638 paragraph before, but the incubation with smiFISH probes was carried on overnight to
639 better allow the detection of incoming genomic viral RNA in CPSF6 clusters (Fig.S4).
640 Confocal microscopy was carried out with a Zeiss LSM700 inverted microscope, with
641 a 63X objective (Plan Apochromat, oil immersion, NA=1.4).

642 **Time-lapse microscopy**

643 For all live imaging studies, 10^5 cells were plated on a polymer-coverslip bottom μ -Dish
644 35 mm (ibidi #81156) at least 24 hours before 2D or 3D video acquisition with an
645 UltraView VOX inverted Microscope (Perkin-Elmer), based on a CSU-X spinning-disk
646 (Yokogawa), and using a 63X objective (Plan Apochromat, oil immersion, NA=1.4). For
647 integrated provirus imaging, HIV-1 ANCH3 single-cell clone was transduced with OR-
648 GFP LV (MOI 0.2) for 3 days and then plated on the polymer-bottom dish the day
649 before acquisition. On the other hand, HeLa P4R5 cells were infected with HIV-1
650 ANCH3 (MOI 10) and five days post infection cells were plated on the polymer-
651 coverslip bottom dish and transduced with LV OR-GFP for 24h. For the acquisitions of
652 the episomal viral DNA, HeLa P4R5 were firstly transduced with OR-GFP LV (MOI 0.2)
653 and the day after cells were plated on the polymer-bottom dish and infected with HIV-
654 1 ANCH3 (MOI 10) with RAL 20 μ M or with the HIV-1 ANCH3 IN_{D116A}. Cells were
655 imaged in 3D in continue for 10 minutes. Experiments of co-live tracking of IN-Ruby
656 (GIR) and vDNA (OR-GFP) were performed in HeLa P4R5 cells transduced with LV
657 OR-GFP (MOI 0.2). The following day, cells were infected with HIV-1 ANCH3 IN_{D116A}
658 complemented with the GIR plasmid using an MOI 50. Frames were acquired every
659 30 seconds in 2D video (Fig. S3, video 5) and every minute for 3D videos (Fig. 4B,
660 video 6,7), at different times post infection. For co-live-imaging of vDNA (OR-
661 SANTAKA) and vRNA foci (MCP-GFP), HeLa MCP-GFP cells were transduced with
662 OR-SANTAKA LV (MOI 1) and 24 h later infected with HIV-1 ANCH3 MS2 (MOI 50).

663

664 **Chromatin Immunoprecipitation with qPCR**

665 Four hundred million of THP-1 cells infected with HIV-1 (MOI 5) or uninfected were
666 fixed with 1% formaldehyde for 15 min and quenched with 0.125 M glycine, then sent
667 to Active Motif Services (Carlsbad, CA) to be processed for ChIP-qPCR. In brief,
668 chromatin was isolated by the addition of lysis buffer, followed by disruption with a
669 Dounce homogenizer. Lysates were sonicated and the DNA sheared to an average
670 length of 300-500 bp. Genomic DNA (Input) was prepared by treating aliquots of
671 chromatin with RNase, proteinase K and heat for de-crosslinking, followed by ethanol
672 precipitation. Pellets were resuspended and the resulting DNA was quantified on a
673 NanoDrop spectrophotometer. Extrapolation to the original chromatin volume allowed
674 quantitation of the total chromatin yield. An aliquot of chromatin (40 μ g) was precleared
675 with protein A agarose beads (Invitrogen). Genomic DNA regions of interest were
676 isolated using 4 μ g of antibody against CPSF6 (#NBP1-85676). Complexes were

677 washed, eluted from the beads with SDS buffer, and subjected to RNase and
678 proteinase K treatment. Crosslinks were reversed by incubation overnight at 65°C, and
679 ChIP DNA was purified by phenol-chloroform extraction and ethanol precipitation.
680 Quantitative PCR (qPCR) reactions were carried out in triplicate on specific genomic
681 regions using SYBR Green SuperMix (BioRad). The resulting signals were normalized
682 for primer efficiency by carrying out qPCR for each primer pair using Input DNA.
683 Different RT products were amplified using the following primers, early RT products:
684 5'-GCCTCAATAAAGCTTGCCTTGA-3' and 5'-TGACTAAAAGGGTCTGAGGGATCT-
685 3'; intermediate RT products: 5' -CTAGAACGATTCGCAGTTAATCCT-3' and 5' -CTAT
686 CCTTTGAT GCACACAATAGAG-3'; late RT products: 5'-
687 TGTGTGCCCGTCTGTTGTGT-3' and 5'-GAGTCCTGCGTCGAGAGAGC-3'. De-
688 crosslinked ChIP products were checked by western blot against CPSF6, loading 37.5
689 ng of DNA per sample.

690

691 **Imaging Analysis and Statistics**

692 All data were analyzed in GraphPad Prism 8 (GraphPad Software, La Jolla California
693 USA, www.graphpad.com). All images and videos were analyzed in Fiji (Schindelin et
694 al., 2012) and Icy version 2.0.3.0 (de Chaumont et al., 2012) software. Here below the
695 custom-made protocols:

696 Particle tracking and MSD measurement

697 3D videos were analyzed in Fiji (Schindelin et al., 2012) and viral nuclear particles
698 were tracked along time in 3D using TrackMate plugin (Tinevez et al., 2017). The
699 resulting tracks were exported in MATLAB (The MathWorks, Natick, USA) and then
700 used for mean-squared displacement (MSD) analysis with @msdanalyzer (Tarantino
701 et al., 2014). MSD curves were fitted by a straight line from which we derived the value
702 of the diffusion coefficient: $D = a / (2 * nDim)$, where « a » is the slope of the MSD curve
703 and « nDim » the dimensionality of the image. MSD curves for which the R^2 value was
704 lower than 0.8 were discarded from analysis. Only the initial 25% of the MSD curves
705 were used for the linear fit.

706 vDNA spot intensity analysis

707 The 2D confocal images were analysed with Icy software version 2.0.3.0 (de
708 Chaumont et al., 2012) using a custom made protocol
709 (<http://icy.bioimageanalysis.org/protocol/batch-spots-detections-and-statistics> and
710 doi: 10.5281/zenodo.3925262, example of HeLa confocal image available at doi:

711 10.5281/zenodo.3925213). vDNA spots were detected extracting the green channel
712 and applying first a median filter of half size = 1 and then 3, the Spot Detector with a
713 scale of 1 (sensitivity to 55) on the nuclear ROI only. Data from the spot detection (e.g.
714 mean fluorescence intensity) were exported for analysis. vRNA mean fluorescence
715 intensity signal was computed from the nuclei ROI.

716 vDNA-vRNA association analysis

717 For vDNA - vRNA association studies in Jurkat cells, 3D confocal images were
718 analyzed in Icy version 2.0.3.0 using two successive custom made protocols (first
719 protocol:[http://icy.bioimageanalysis.org/protocol/nuclei-segmentation-from-maximum-
720 intensity-projections/](http://icy.bioimageanalysis.org/protocol/nuclei-segmentation-from-maximum-intensity-projections/) with doi: 10.5281/zenodo.3925181) and second protocol:
721 [http://icy.bioimageanalysis.org/protocol/spots-detection-and-colocalisation-analysis-
722 with-soda/](http://icy.bioimageanalysis.org/protocol/spots-detection-and-colocalisation-analysis-with-soda/) with doi: 10.5281/zenodo.3925191, example of Jurkat confocal image
723 available at doi: 10.5281/zenodo.3925213). Nuclei were segmented on a maximum
724 intensity projection of the Hoechst channel using the Icy block Gaussian filter with a
725 radius of sigma x=5, y=5 and z=5 pixels, the Thresholder block with a manual threshold
726 of 5000 and the Label Extractor block, which uses connected components to separate
727 the nuclei. Cy5 spots were detected with the HK Means block (Dufour et al.,
728 doi.org/10.1109/ICPR.2008.4761748).The logical operation block was used to keep
729 only the spots detected in the nucleus. These spots were added as input parameter
730 “List detection 1” of the SODA block. EGFP spots were detected using the log3D block
731 to enhance the spots, inverting the log transformed image using the Math Operation
732 Expression block with the following expression: $A*B$ with A scalar=-1 and B the log
733 transformed image, detecting the spots with the Local Extrema block and segmenting
734 the spots with a dilation and a connected components operations. The logical operation
735 block was used to keep only the spots detected in the nucleus. These spots were
736 added as input parameter “List detection 2” of the SODA block. The nucleus ROI was
737 kept as input parameter for “ROI of Analysis (Cell’s shape)”. The Cy5 and GFP spots
738 ROIs were then imported in the SODA block (Lagache et al., 2018) to analyse
739 colocalization of spots within the nucleus only with a maximum radius of 10, a step of
740 1 and no fixed search distance.

741 vDNA/vRNA nuclear envelope distance analysis

742 The nuclei were segmented on the Hoechst channel using background subtraction
743 followed by a multilevel Otsu thresholding. The resulting nuclei masks were then
744 directly applied on the vDNA and vRNA channels to select the relevant 3D information

745 inside each labelled region. Inside these regions, vRNA spots were identified using 3D
746 non-local means denoising (Buades et al., "Non-local means denoising." *Image*
747 *Processing On Line 1* (2011): 208-212) and automated segmentation, while vDNA
748 spots were extracted with the image analysis pipeline previously described (Komatsu
749 et al., 2018). For each vDNA and vRNA spot in was computed the distance to the
750 nuclear envelope in the 2D z-plane corresponding to the spot centroid location.

751 SC35/HIV-1 MLO distances analysis

752 The 3D confocal images were processed for multi-channel image splitting, vDNA and
753 SC35 segmentation. The automated 3D segmentation of cell nuclei included a
754 preliminary non-local means denoising step to cope with the strong signal
755 heterogeneity and the segmentation of SC35 was readjusted to low contrast
756 conditions. The 3D boundary-to-boundary distance (rather than centroid-to-centroid
757 which was done for vDNA/vRNA-NE analysis) between each vDNA or vRNA spot and
758 its closest SC35 speckle or the closest HIV-1 MLO (SC35+CPSF6) were computed.

759

760 **Acknowledgements**

761 We wish to thank Guillermo Blanco-Rodriguez, Stella Frabetti, Philippe Souque and
762 Blandine Monel for experimental help, Nicoletta Casartelli for critical reading of the
763 manuscript. We thank Fabrizio Mammano, Edouard Bertrand, Florian Mueller, and
764 Edward Campbell for sharing reagents. We gratefully acknowledge the UtechS
765 Photonic Biolmaging (Imagopole), C2RT, Institut Pasteur, supported by the French
766 National Research Agency (France Biolmaging; ANR-10-INSB-04; Investments for
767 the Future). We thank the NIH AIDS Reagents program to support us with precious
768 reagents. This work was funded by the ANRS REACTing grant ECTZ88162 with a
769 nominative PhD student fellowship ECTZ88177 for V.S., the Sidaction/FRM grant
770 VIH20170718001, the Pasteur Institute.

771

772 **Competing financial interests:** The authors declare no competing financial interests.

773

774 **References**

775 Achuthan, V., J.M. Ferreira, G.A. Sowd, M. Puray-Chavez, W.M. McDougall, A. Paulucci-Holthauzen, X.
776 Wu, H.J. Fadel, E.M. Poeschla, A.S. Multani, S.H. Hughes, S.G. Sarafianos, A.L. Brass, and A.N.

- 777 Engelman. 2018. Capsid-CPSF6 Interaction Licenses Nuclear HIV-1 Trafficking to Sites of Viral
778 DNA Integration. *Cell Host Microbe*. 24:392-404 e398.
- 779 Albanese, A., D. Arosio, M. Terreni, and A. Cereseto. 2008. HIV-1 pre-integration complexes selectively
780 target decondensed chromatin in the nuclear periphery. *PLoS One*. 3:e2413.
- 781 Ballandras-Colas, A., D.P. Maskell, E. Serrao, J. Locke, P. Swuec, S.R. Jonsson, A. Kotecha, N.J. Cook, V.E.
782 Pye, I.A. Taylor, V. Andresdottir, A.N. Engelman, A. Costa, and P. Cherepanov. 2017. A
783 supramolecular assembly mediates lentiviral DNA integration. *Science*. 355:93-95.
- 784 Bejarano, D.A., K. Peng, V. Laketa, K. Borner, K.L. Jost, B. Lucic, B. Glass, M. Lusic, B. Muller, and H.G.
785 Krausslich. 2019. HIV-1 nuclear import in macrophages is regulated by CPSF6-capsid
786 interactions at the nuclear pore complex. *Elife*. 8.
- 787 Blanco-Rodriguez, G., A. Gazi, B. Monel, S. Frabetti, V. Scoca, F. Mueller, O. Schwartz, J. Krijnse-Locker,
788 P. Charneau, and F. Di Nunzio. 2020. Remodeling of the core leads HIV-1 pre-integration
789 complex in the nucleus of human lymphocytes. *J Virol*.
- 790 Buffone, C., A. Martinez-Lopez, T. Fricke, S. Opp, M. Severgnini, I. Cifola, L. Petiti, S. Frabetti, K.
791 Skorupka, K.K. Zadrozny, B.K. Ganser-Pornillos, O. Pornillos, F. Di Nunzio, and F. Diaz-Griffero.
792 2018. Nup153 Unlocks the Nuclear Pore Complex for HIV-1 Nuclear Translocation in
793 Nondividing Cells. *J Virol*. 92.
- 794 Burdick, R.C., K.A. Delviks-Frankenberry, J. Chen, S.K. Janaka, J. Sastri, W.S. Hu, and V.K. Pathak. 2017.
795 Dynamics and regulation of nuclear import and nuclear movements of HIV-1 complexes. *PLoS*
796 *Pathog*. 13:e1006570.
- 797 Burdick, R.C., C. Li, M. Munshi, J.M.O. Rawson, K. Nagashima, W.S. Hu, and V.K. Pathak. 2020. HIV-1
798 uncoats in the nucleus near sites of integration. *Proc Natl Acad Sci U S A*. 117:5486-5493.
- 799 Bushman, F.D. 2003. Targeting survival: integration site selection by retroviruses and LTR-
800 retrotransposons. *Cell*. 115:135-138.
- 801 Butler, S.L., M.S. Hansen, and F.D. Bushman. 2001. A quantitative assay for HIV DNA integration in vivo.
802 *Nat Med*. 7:631-634.
- 803 Campbell, E.M., and T.J. Hope. 2015. HIV-1 capsid: the multifaceted key player in HIV-1 infection. *Nat*
804 *Rev Microbiol*. 13:471-483.
- 805 Charneau, P., G. Mirambeau, P. Roux, S. Paulous, H. Buc, and F. Clavel. 1994. HIV-1 reverse
806 transcription. A termination step at the center of the genome. *J Mol Biol*. 241:651-662.
- 807 Cherepanov, P., G. Maertens, P. Proost, B. Devreese, J. Van Beeumen, Y. Engelborghs, E. De Clercq,
808 and Z. Debyser. 2003. HIV-1 integrase forms stable tetramers and associates with LEDGF/p75
809 protein in human cells. *J Biol Chem*. 278:372-381.
- 810 Chin, C.R., J.M. Perreira, G. Savidis, J.M. Portmann, A.M. Aker, E.M. Feeley, M.C. Smith, and A.L. Brass.
811 2015. Direct Visualization of HIV-1 Replication Intermediates Shows that Capsid and CPSF6
812 Modulate HIV-1 Intra-nuclear Invasion and Integration. *Cell Rep*. 13:1717-1731.
- 813 Ciuffi, A., M. Llano, E. Poeschla, C. Hoffmann, J. Leipzig, P. Shinn, J.R. Ecker, and F. Bushman. 2005. A
814 role for LEDGF/p75 in targeting HIV DNA integration. *Nat Med*. 11:1287-1289.
- 815 Craig, E.A., and J. Marszalek. 2002. A specialized mitochondrial molecular chaperone system: a role in
816 formation of Fe/S centers. *Cell Mol Life Sci*. 59:1658-1665.
- 817 de Chaumont, F., S. Dallongeville, N. Chenouard, N. Herve, S. Pop, T. Provoost, V. Meas-Yedid, P.
818 Pankajakshan, T. Lecomte, Y. Le Montagner, T. Lagache, A. Dufour, and J.C. Olivo-Marin. 2012.
819 Icy: an open bioimage informatics platform for extended reproducible research. *Nat Methods*.
820 9:690-696.
- 821 De Wit, F., S.R. Pillalamarri, A. Sebastian-Martin, A. Venkatesham, A. Van Aerschot, and Z. Debyser.
822 2019. Design of reverse transcriptase-specific nucleosides to visualize early steps of HIV-1
823 replication by click labeling. *J Biol Chem*. 294:11863-11875.
- 824 Dharan, A., S. Talley, A. Tripathi, J.I. Mamede, M. Majetschak, T.J. Hope, and E.M. Campbell. 2016.
825 KIF5B and Nup358 Cooperatively Mediate the Nuclear Import of HIV-1 during Infection. *PLoS*
826 *Pathog*. 12:e1005700.
- 827 Di Nunzio, F. 2013. New insights in the role of nucleoporins: a bridge leading to concerted steps from
828 HIV-1 nuclear entry until integration. *Virus Res*. 178:187-196.

- 829 Di Nunzio, F., T. Fricke, A. Miccio, J.C. Valle-Casuso, P. Perez, P. Souque, E. Rizzi, M. Severgnini, F.
830 Mavilio, P. Charneau, and F. Diaz-Griffero. 2013. Nup153 and Nup98 bind the HIV-1 core and
831 contribute to the early steps of HIV-1 replication. *Virology*. 440:8-18.
- 832 Di Primio, C., V. Quercioli, A. Allouch, R. Gijssbers, F. Christ, Z. Debyser, D. Arosio, and A. Cereseto. 2013.
833 Single-cell imaging of HIV-1 provirus (SCIP). *Proc Natl Acad Sci U S A*. 110:5636-5641.
- 834 Durand, S., X.N. Nguyen, J. Turpin, S. Cordeil, N. Nazaret, S. Croze, R. Mahieux, J. Lachuer, C. Legras-
835 Lachuer, and A. Cimorelli. 2013. Tailored HIV-1 vectors for genetic modification of primary
836 human dendritic cells and monocytes. *J Virol*. 87:234-242.
- 837 Emiliani, S., A. Mousnier, K. Busschots, M. Maroun, B. Van Maele, D. Tempe, L. Vandekerckhove, F.
838 Moisant, L. Ben-Slama, M. Witvrouw, F. Christ, J.C. Rain, C. Dargemont, Z. Debyser, and R.
839 Benarous. 2005. Integrase mutants defective for interaction with LEDGF/p75 are impaired in
840 chromosome tethering and HIV-1 replication. *J Biol Chem*. 280:25517-25523.
- 841 Farnet, C.M., and W.A. Haseltine. 1991. Determination of viral proteins present in the human
842 immunodeficiency virus type 1 preintegration complex. *J Virol*. 65:1910-1915.
- 843 Ferris, A.L., X. Wu, C.M. Hughes, C. Stewart, S.J. Smith, T.A. Milne, G.G. Wang, M.C. Shun, C.D. Allis, A.
844 Engelman, and S.H. Hughes. 2010. Lens epithelium-derived growth factor fusion proteins
845 redirect HIV-1 DNA integration. *Proc Natl Acad Sci U S A*. 107:3135-3140.
- 846 Fox, A.H., Y.W. Lam, A.K. Leung, C.E. Lyon, J. Andersen, M. Mann, and A.I. Lamond. 2002. Paraspeckles:
847 a novel nuclear domain. *Curr Biol*. 12:13-25.
- 848 Francis, A.C., C. Di Primio, V. Quercioli, P. Valentini, A. Boll, G. Girelli, F. Demichelis, D. Arosio, and A.
849 Cereseto. 2014. Second generation imaging of nuclear/cytoplasmic HIV-1 complexes. *AIDS Res
850 Hum Retroviruses*. 30:717-726.
- 851 Francis, A.C., M. Marin, J. Shi, C. Aiken, and G.B. Melikyan. 2016. Time-Resolved Imaging of Single HIV-
852 1 Uncoating In Vitro and in Living Cells. *PLoS Pathog*. 12:e1005709.
- 853 Francis, A.C., M. Marin, P.K. Singh, V. Achuthan, M.J. Prellberg, K. Palermi-Rowland, S. Lan, P.R.
854 Tedbury, S.G. Sarafianos, A.N. Engelman, and G.B. Melikyan. 2020. HIV-1 replication
855 complexes accumulate in nuclear speckles and integrate into speckle-associated genomic
856 domains. *Nat Commun*. 11:3505.
- 857 Francis, A.C., and G.B. Melikyan. 2018. Single HIV-1 Imaging Reveals Progression of Infection through
858 CA-Dependent Steps of Docking at the Nuclear Pore, Uncoating, and Nuclear Transport. *Cell
859 Host Microbe*. 23:536-548 e536.
- 860 Geis, F.K., and S.P. Goff. 2019. Unintegrated HIV-1 DNAs are loaded with core and linker histones and
861 transcriptionally silenced. *Proc Natl Acad Sci U S A*. 116:23735-23742.
- 862 Germier, T., S. Kocanova, N. Walther, A. Bancaud, H.A. Shaban, H. Sellou, A.Z. Politi, J. Ellenberg, F.
863 Gallardo, and K. Bystrycky. 2017. Real-Time Imaging of a Single Gene Reveals Transcription-
864 Initiated Local Confinement. *Biophys J*. 113:1383-1394.
- 865 Graham, T.G., X. Wang, D. Song, C.M. Etson, A.M. van Oijen, D.Z. Rudner, and J.J. Loparo. 2014. ParB
866 spreading requires DNA bridging. *Genes Dev*. 28:1228-1238.
- 867 Greig, J.A., T.A. Nguyen, M. Lee, A.S. Holehouse, A.E. Posey, R.V. Pappu, and G. Jedd. 2020. Arginine-
868 Enriched Mixed-Charge Domains Provide Cohesion for Nuclear Speckle Condensation. *Mol
869 Cell*. 77:1237-1250 e1234.
- 870 Hare, S., F. Di Nunzio, A. Labeja, J. Wang, A. Engelman, and P. Cherepanov. 2009. Structural basis for
871 functional tetramerization of lentiviral integrase. *PLoS Pathog*. 5:e1000515.
- 872 Hrecka, K., C. Hao, M. Gierszewska, S.K. Swanson, M. Kesik-Brodacka, S. Srivastava, L. Florens, M.P.
873 Washburn, and J. Skowronski. 2011. Vpx relieves inhibition of HIV-1 infection of macrophages
874 mediated by the SAMHD1 protein. *Nature*. 474:658-661.
- 875 Hubner, W., G.P. McNeerney, P. Chen, B.M. Dale, R.E. Gordon, F.Y. Chuang, X.D. Li, D.M. Asmuth, T.
876 Huser, and B.K. Chen. 2009. Quantitative 3D video microscopy of HIV transfer across T cell
877 virological synapses. *Science*. 323:1743-1747.
- 878 Hulme, A.E., Z. Kelley, D. Foley, and T.J. Hope. 2015. Complementary Assays Reveal a Low Level of CA
879 Associated with Viral Complexes in the Nuclei of HIV-1-Infected Cells. *J Virol*. 89:5350-5361.

- 880 Komatsu, T., C. Quentin-Froignant, I. Carlon-Andres, F. Lagadec, F. Rayne, J. Ragues, R.H. Kehlenbach,
881 W. Zhang, A. Ehrhardt, K. Bystricky, R. Morin, J.M. Lagarde, F. Gallardo, and H. Wodrich. 2018.
882 In Vivo Labelling of Adenovirus DNA Identifies Chromatin Anchoring and Biphasic Genome
883 Replication. *J Virol.* 92.
- 884 Lagache, T., A. Grassart, S. Dallongeville, O. Faklaris, N. Sauvonnnet, A. Dufour, L. Danglot, and J.C. Olivo-
885 Marin. 2018. Mapping molecular assemblies with fluorescence microscopy and object-based
886 spatial statistics. *Nat Commun.* 9:698.
- 887 Laguette, N., B. Sobhian, N. Casartelli, M. Ringiard, C. Chable-Bessia, E. Segeral, A. Yatim, S. Emiliani,
888 O. Schwartz, and M. Benkirane. 2011. SAMHD1 is the dendritic- and myeloid-cell-specific HIV-
889 1 restriction factor counteracted by Vpx. *Nature.* 474:654-657.
- 890 Lamond, A.I., and D.L. Spector. 2003. Nuclear speckles: a model for nuclear organelles. *Nat Rev Mol*
891 *Cell Biol.* 4:605-612.
- 892 Lee, K., Z. Ambrose, T.D. Martin, I. Oztop, A. Mulky, J.G. Julias, N. Vandegraaff, J.G. Baumann, R. Wang,
893 W. Yuen, T. Takemura, K. Shelton, I. Taniuchi, Y. Li, J. Sodroski, D.R. Littman, J.M. Coffin, S.H.
894 Hughes, D. Unutmaz, A. Engelman, and V.N. KewalRamani. 2010. Flexible use of nuclear import
895 pathways by HIV-1. *Cell Host Microbe.* 7:221-233.
- 896 Lelek, M., N. Casartelli, D. Pellin, E. Rizzi, P. Souque, M. Severgnini, C. Di Serio, T. Fricke, F. Diaz-Griffero,
897 C. Zimmer, P. Charneau, and F. Di Nunzio. 2015. Chromatin organization at the nuclear pore
898 favours HIV replication. *Nat Commun.* 6:6483.
- 899 Lelek, M., F. Di Nunzio, R. Henriques, P. Charneau, N. Arhel, and C. Zimmer. 2012. Superresolution
900 imaging of HIV in infected cells with FIAsh-PALM. *Proc Natl Acad Sci U S A.* 109:8564-8569.
- 901 Liu, R., F.R. Simonetti, and Y.C. Ho. 2020. The forces driving clonal expansion of the HIV-1 latent
902 reservoir. *Viol J.* 17:4.
- 903 Llano, M., D.T. Saenz, A. Meehan, P. Wongthida, M. Peretz, W.H. Walker, W. Teo, and E.M. Poeschla.
904 2006. An essential role for LEDGF/p75 in HIV integration. *Science.* 314:461-464.
- 905 Maldarelli, F. 2016. The role of HIV integration in viral persistence: no more whistling past the proviral
906 graveyard. *J Clin Invest.* 126:438-447.
- 907 Mamede, J.I., G.C. Cianci, M.R. Anderson, and T.J. Hope. 2017. Early cytoplasmic uncoating is
908 associated with infectivity of HIV-1. *Proc Natl Acad Sci U S A.* 114:E7169-E7178.
- 909 Mariame, B., S. Kappler-Gratias, M. Kappler, S. Balor, F. Gallardo, and K. Bystricky. 2018. Real-Time
910 Visualization and Quantification of Human Cytomegalovirus Replication in Living Cells Using
911 the ANCHOR DNA Labeling Technology. *J Virol.* 92.
- 912 Marini, B., A. Kertesz-Farkas, H. Ali, B. Lucic, K. Lisek, L. Manganaro, S. Pongor, R. Luzzati, A. Recchia, F.
913 Mavilio, M. Giacca, and M. Lusic. 2015. Nuclear architecture dictates HIV-1 integration site
914 selection. *Nature.* 521:227-231.
- 915 Naganuma, T., and T. Hirose. 2013. Paraspeckle formation during the biogenesis of long non-coding
916 RNAs. *RNA Biol.* 10:456-461.
- 917 Olson, A., B. Basukala, W.W. Wong, and A.J. Henderson. 2019. Targeting HIV-1 proviral transcription.
918 *Curr Opin Virol.* 38:89-96.
- 919 Peng, K., W. Muranyi, B. Glass, V. Laketa, S.R. Yant, L. Tsai, T. Cihlar, B. Muller, and H.G. Krausslich.
920 2014. Quantitative microscopy of functional HIV post-entry complexes reveals association of
921 replication with the viral capsid. *Elife.* 3:e04114.
- 922 Petit, C., O. Schwartz, and F. Mammano. 1999. Oligomerization within virions and subcellular
923 localization of human immunodeficiency virus type 1 integrase. *J Virol.* 73:5079-5088.
- 924 Petit, C., O. Schwartz, and F. Mammano. 2000. The karyophilic properties of human immunodeficiency
925 virus type 1 integrase are not required for nuclear import of proviral DNA. *J Virol.* 74:7119-
926 7126.
- 927 Pradeepa, M.M., G.R. Grimes, G.C. Taylor, H.G. Sutherland, and W.A. Bickmore. 2014. Psp1/Ledgf p75
928 restrains Hox gene expression by recruiting both trithorax and polycomb group proteins.
929 *Nucleic Acids Res.* 42:9021-9032.

- 930 Pradeepa, M.M., H.G. Sutherland, J. Ule, G.R. Grimes, and W.A. Bickmore. 2012. Psp1/Ledgf p52 binds
931 methylated histone H3K36 and splicing factors and contributes to the regulation of alternative
932 splicing. *PLoS Genet.* 8:e1002717.
- 933 Price, A.J., D.A. Jacques, W.A. McEwan, A.J. Fletcher, S. Essig, J.W. Chin, U.D. Halambage, C. Aiken, and
934 L.C. James. 2014. Host cofactors and pharmacologic ligands share an essential interface in HIV-
935 1 capsid that is lost upon disassembly. *PLoS Pathog.* 10:e1004459.
- 936 Rensen, E., F. Mueller, V. Scoca, J.J. Parmar, P. Souque, C. Zimmer, and F. Di Nunzio. 2020. Clustering
937 and reverse transcription of HIV-1 genomes in nuclear niches of macrophages. *EMBO J.*
938 *J:e105247.*
- 939 Rensen, E., F. Mueller, V. Scoca, J.J. Parmar, P. Souque, C. Zimmer, and F. Di Nunzio. 2021. Clustering
940 and reverse transcription of HIV-1 genomes in nuclear niches of macrophages. *EMBO J.*
941 *40:e105247.*
- 942 Saad, H., F. Gallardo, M. Dalvai, N. Tanguy-le-Gac, D. Lane, and K. Bystricky. 2014. DNA dynamics during
943 early double-strand break processing revealed by non-intrusive imaging of living cells. *PLoS*
944 *Genet.* 10:e1004187.
- 945 Sanchez, A., D.I. Cattoni, J.C. Walter, J. Rech, A. Parmeggiani, M. Nollmann, and J.Y. Bouet. 2015.
946 Stochastic Self-Assembly of ParB Proteins Builds the Bacterial DNA Segregation Apparatus. *Cell*
947 *Syst.* 1:163-173.
- 948 Schindelin, J., I. Arganda-Carreras, E. Frise, V. Kaynig, M. Longair, T. Pietzsch, S. Preibisch, C. Rueden,
949 S. Saalfeld, B. Schmid, J.Y. Tinevez, D.J. White, V. Hartenstein, K. Eliceiri, P. Tomancak, and A.
950 Cardona. 2012. Fiji: an open-source platform for biological-image analysis. *Nat Methods.*
951 *9:676-682.*
- 952 Schroder, A.R., P. Shinn, H. Chen, C. Berry, J.R. Ecker, and F. Bushman. 2002. HIV-1 integration in the
953 human genome favors active genes and local hotspots. *Cell.* 110:521-529.
- 954 Scoca, V., and F. Di Nunzio. 2021a. The HIV-1 Capsid: From Structural Component to Key Factor for
955 Host Nuclear Invasion. *Viruses.* 13.
- 956 Scoca, V., and F. Di Nunzio. 2021b. Membraneless organelles restructured and built by pandemic
957 viruses: HIV-1 and SARS-CoV-2. *J Mol Cell Biol.*
- 958 Sharkey, M., D.Z. Babic, T. Greenough, R. Gulick, D.R. Kuritzkes, and M. Stevenson. 2011. Episomal viral
959 cDNAs identify a reservoir that fuels viral rebound after treatment interruption and that
960 contributes to treatment failure. *PLoS Pathog.* 7:e1001303.
- 961 Sharkey, M.E., I. Teo, T. Greenough, N. Sharova, K. Luzuriaga, J.L. Sullivan, R.P. Bucy, L.G. Kostrikis, A.
962 Haase, C. Veryard, R.E. Davaro, S.H. Cheeseman, J.S. Daly, C. Bova, R.T. Ellison, 3rd, B. Mady,
963 K.K. Lai, G. Moyle, M. Nelson, B. Gazzard, S. Shaunak, and M. Stevenson. 2000. Persistence of
964 episomal HIV-1 infection intermediates in patients on highly active anti-retroviral therapy. *Nat*
965 *Med.* 6:76-81.
- 966 Shun, M.C., Y. Botbol, X. Li, F. Di Nunzio, J.E. Daigle, N. Yan, J. Lieberman, M. Lavigne, and A. Engelman.
967 2008. Identification and characterization of PWWP domain residues critical for LEDGF/p75
968 chromatin binding and human immunodeficiency virus type 1 infectivity. *J Virol.* 82:11555-
969 11567.
- 970 Shun, M.C., N.K. Raghavendra, N. Vandegraaff, J.E. Daigle, S. Hughes, P. Kellam, P. Cherepanov, and A.
971 Engelman. 2007. LEDGF/p75 functions downstream from preintegration complex formation to
972 effect gene-specific HIV-1 integration. *Genes Dev.* 21:1767-1778.
- 973 Singh, P.K., M.R. Plumb, A.L. Ferris, J.R. Iben, X. Wu, H.J. Fadel, B.T. Luke, C. Esnault, E.M. Poeschla, S.H.
974 Hughes, M. Kvaratskhelia, and H.L. Levin. 2015. LEDGF/p75 interacts with mRNA splicing
975 factors and targets HIV-1 integration to highly spliced genes. *Genes Dev.* 29:2287-2297.
- 976 Spector, D.L., and A.I. Lamond. 2011. Nuclear speckles. *Cold Spring Harb Perspect Biol.* 3.
- 977 Stultz, R.D., J.J. Cenker, and D. McDonald. 2017. Imaging HIV-1 Genomic DNA from Entry through
978 Productive Infection. *J Virol.* 91.
- 979 Suzuki, Y., and R. Craigie. 2007. The road to chromatin - nuclear entry of retroviruses. *Nat Rev*
980 *Microbiol.* 5:187-196.

981 Tantale, K., F. Mueller, A. Kozulic-Pirher, A. Lesne, J.M. Victor, M.C. Robert, S. Capozzi, R. Chouaib, V.
982 Backer, J. Mateos-Langerak, X. Darzacq, C. Zimmer, E. Basyuk, and E. Bertrand. 2016. A single-
983 molecule view of transcription reveals convoys of RNA polymerases and multi-scale bursting.
984 *Nat Commun.* 7:12248.

985 Tarantino, N., J.Y. Tinevez, E.F. Crowell, B. Boisson, R. Henriques, M. Mhlanga, F. Agou, A. Israel, and E.
986 Laplantine. 2014. TNF and IL-1 exhibit distinct ubiquitin requirements for inducing NEMO-IKK
987 supramolecular structures. *J Cell Biol.* 204:231-245.

988 Tinevez, J.Y., N. Perry, J. Schindelin, G.M. Hoopes, G.D. Reynolds, E. Laplantine, S.Y. Bednarek, S.L.
989 Shorte, and K.W. Eliceiri. 2017. TrackMate: An open and extensible platform for single-particle
990 tracking. *Methods.* 115:80-90.

991 Tsanov, N., A. Samacoits, R. Chouaib, A.M. Traboulsi, T. Gostan, C. Weber, C. Zimmer, K. Zibara, T.
992 Walter, M. Peter, E. Bertrand, and F. Mueller. 2016. smiFISH and FISH-quant - a flexible single
993 RNA detection approach with super-resolution capability. *Nucleic Acids Res.* 44:e165.

994 Vansant, G., H.C. Chen, E. Zorita, K. Trejbalova, D. Miklik, G. Filion, and Z. Debyser. 2020. The chromatin
995 landscape at the HIV-1 provirus integration site determines viral expression. *Nucleic Acids Res.*

996 Wang, G.P., B.L. Levine, G.K. Binder, C.C. Berry, N. Malani, G. McGarrity, P. Tebas, C.H. June, and F.D.
997 Bushman. 2009. Analysis of lentiviral vector integration in HIV+ study subjects receiving
998 autologous infusions of gene modified CD4+ T cells. *Mol Ther.* 17:844-850.

999 Wang, H., M.C. Shun, X. Li, F. Di Nunzio, S. Hare, P. Cherepanov, and A. Engelman. 2014. Efficient
1000 Transduction of LEDGF/p75 Mutant Cells by Gain-of-Function HIV-1 Integrase Mutant Viruses.
1001 *Mol Ther Methods Clin Dev.* 1.

1002 Zhu, Y., G.Z. Wang, O. Cingoz, and S.P. Goff. 2018. NP220 mediates silencing of unintegrated retroviral
1003 DNA. *Nature.* 564:278-282.

1004

1005

1006

1007

1008
1009
1010
1011
1012
1013
1014
1015
1016
1017
1018
1019
1020
1021
1022
1023
1024
1025
1026
1027
1028
1029
1030
1031
1032
1033

FIGURE LEGENDS

Figure 1. Detection and live tracking of nuclear HIV-1 DNA forms. A) Scheme of HIV-1 ANCHOR system created with BioRender.com. ANCH3 sequence has been cloned in the HIV-1 genome in place of Nef gene (HIV-1 ANCH3). The late retrotranscribed DNA of HIV-1 ANCH3 can be visualized in cells stably expressing the OR-GFP protein, thanks to OR accumulation on the double-stranded ANCH3 sequence. Viral DNA detection occurs mostly in the nucleus, where late reverse transcripts are abundant and are more likely to be exposed to the binding of OR-GFP. Starting from early time points of infection, it is possible to follow HIV-1 ANCH3 in target cells. The labelling results in the appearance of a bright fluorescent spot that can be tracked over time post infection. **B)** Confocal images of HeLa P4R5 cells expressing OR-GFP infected with HIV-1 ANCH3 (MOI 30), HIV-1 ANCH3 + RAL (20 μ M), HIV-1 ANCH3 IN_{D116A} and HIV-1 ANCH3 + NEV (10 μ M), 24 h p.i. The histogram plots of 2-LTR circles and ALU-PCR represent the nuclear import and integration rates, respectively. One-way ANOVA followed by Turkey's multiple comparison test, ns=non-significant, ****= $p \leq 0.0001$. **C)** Confocal image of HIV-1 ANCH3 provirus in a single-cell clone. The clone was transduced with OR-GFP LV for the detection of HIV-1 integrated DNA. On the right, histogram plot of ALU-PCR and β -galactosidase expression of the HIV-1 ANCH3 single-cell clone compared to uninfected cells (NI). Unpaired t test, **= $p \leq 0.01$, ****= $p \leq 0.0001$. **D)** Tukey's box plots of the diffusion coefficient (D (nm^2/s)) of episomal and integrated HIV-1 DNA forms tracked in 3D time lapses (video 1, 2, 3). On the right, an example of the live track for each experimental group is shown. Low D corresponds to D (nm^2/s) < 5 and high D to $5 < D$ (nm^2/s) < 20 . The color range indicates the time up to 10 min. All graphs contain \pm SD. Scale bar: 5 μ m.

1034
1035
1036
1037
1038
1039
1040

Figure 2. HIV-1 transcriptional activity in dividing and non-dividing cells. Co-labeling of vDNA and vRNA by coupling HIV-1 ANCHOR with RNA FISH. A) Confocal images of HIV-1 RNA FISH in HeLa P4R5 cells (MOI 30) with or without RAL (20 μ M), 24 h p.i. The scatter plots with bars show the mean fluorescence intensity of the vRNA signal per nucleus and of vDNA spots (vRNA: 13 (-RAL), 16 (+RAL) cells; vDNA: 95 (-RAL) and 141 (+RAL) spots). The analysis was performed in 2D. Unpaired t test, ****= p

1041 ≤ 0.0001 . **B)** Confocal image of HIV-1 RNA FISH in Jurkat CD4+T cells (MOI 5), 48 h
1042 p.i. The scatter plot with bars shows the percentage of vDNA associated to vRNA
1043 signal and vice versa, per nucleus (12 cells; 262 vDNAs; 64 vRNA foci). The analysis
1044 was performed in 3D. Unpaired t test, $**=p \leq 0.01$. **C)** Confocal image of HIV-1 RNA
1045 FISH in macrophage-like THP-1 cells (MOI 20) 3 days p.i. The scatter plot with bars
1046 shows the percentage of vDNA associated to vRNA signal and vice versa, per nucleus
1047 (8 cells; 130 vDNAs; 99 vRNA foci). The analysis was performed in 3D. Unpaired t test,
1048 $*=p \leq 0.05$. **D)** Confocal image of HIV-1 RNA FISH in primary activated CD4+T cells
1049 (MOI 50), 3 days p.i. and primary monocyte-derived macrophages (MDMs), (MOI 40),
1050 4 days p.i.. All graphs contain \pm SD. Scale bar: 5 μ m.

1051
1052 **Figure 3. Nuclear localization of HIV-1 provirus in dividing and non-dividing**
1053 **cells.** Co-labeling of vDNA and vRNA by coupling of HIV-1 ANCHOR with RNA FISH.
1054 **A)** Confocal images of HIV-1 RNA FISH in HeLa P4R5 cells infected with HIV-1
1055 ANCH3 (MOI 5) at 48 h p.i. compared to 7 days p.i.. The scatter plot with bars indicates
1056 the distance from the nuclear envelope (NE) per detected vDNA spot (green) and
1057 vRNA focus (red) (n cells = 11 (48 h p.i.), 10 (+RAL), 5 (IN_{D116A}), and 9 (7 days p.i.);
1058 vDNA: 83 (48 h p.i.), 87 (+RAL), 29 (IN_{D116A}), 16 (7 d p.i.); vRNA: 52 (48h p.i.) and 18
1059 (7d p.i.)). One-way ANOVA followed by Turkey's multiple comparison test, ns=non-
1060 significant, $*=p \leq 0.05$, $**=p \leq 0.01$. **B)** Confocal image of HIV-1 RNA FISH in THP-1
1061 cells infected with HIV-1 ANCH3 (MOI 20), 3 days p.i.. The scatter plot with bars
1062 indicates the distance from the nuclear envelope (NE) per detected vDNA (green) or
1063 vRNA (red) (n cells = 8 (vDNA, vRNA), 13 (IN_{D116A}); n spots= 139 (vDNA), 76 (IN_{D116A}),
1064 126 (vRNA)). Unpaired t test, $*=p \leq 0.05$, $***=p \leq 0.001$. **C)** Scatter plot with bars
1065 comparing the distances from the NE per detected vRNA focus in HeLa P4R5 and
1066 THP-1 cells (n = 11 (HeLa) and 8 (THP-1) cells; vRNAs: 52 (HeLa) and 126 (THP-1)).
1067 Unpaired t test, ns=non-significant. All the analyses were performed in 3D. All graphs
1068 contain \pm SD. Scale bar: 5 μ m, inset: 1 μ m.

1069
1070 **Figure 4. Sequestration of viral components in CPSF6 clusters.** **A)** Late reverse
1071 transcripts separation from integrase (IN) foci: confocal images of infected primary
1072 activated CD4+ T cells (MOI 100, 20 h p.i.) and macrophage-like cells, THP-1 cell line,
1073 (MOI 10, 30h p.i.), compared to uninfected cells. The scatter plot with bars compares

1074 the percentages of vDNAs associated to IN, per nucleus (CD4+T = 8 cells, 54 vDNAs;
1075 THP-1 = 13 cells, 100 vDNAs). Unpaired t test, ns = non-significant. The analysis was
1076 performed in 3D. **B)** On the left, quantification of IN foci found associated to vDNA
1077 signal for each time-lapse video (at frame 0) (n = 13 cells, 81 IN foci). Six different
1078 videos were performed at sequential time p.i. On the right, example of vDNA
1079 separation in live, tracked down in the 18-hours p.i. video (video 6). Pearson's
1080 correlation per time frame is shown below. **C)** Confocal images of infected primary
1081 activated CD4⁺ T cells (MOI 100, 20 h p.i.) and THP-1 cells (MOI 10, 30h p.i.),
1082 compared to uninfected cells. The graph shows the percentages of IN associated to
1083 CPSF6, per nucleus (CD4⁺T = 12 cells, 33 IN foci; THP-1 = 40 cells, 132 IN foci).
1084 Unpaired t test, ns = non-significant. **D)** Confocal images of Immuno-RNA FISH in
1085 SupT1R5 CD4⁺T cells and THP-1 cells infected with HIV-1 ANCH3 (MOI 20; 2 days
1086 p.i.). The graph shows the percentages of vRNA associated to CPSF6 per condition.
1087 (CD4⁺T = 19 (-NEV), 16 (+NEV) cells, 79 (-NEV), 30 (+NEV) vRNAs; THP-1 = 56 (-
1088 NEV), 34 (+NEV) cells, 151 (-NEV), 61 (+NEV) vRNAs). Unpaired t test, **=p ≤ 0.01,
1089 ****=p ≤ 0.0001. All graphs contain ± SD. Scale bar: 5 μm, inset: 1 μm.

1090
1091 **Figure 5. HIV- MLOs as nuclear hubs of HIV-1 reverse transcription. A)** Confocal
1092 images of Immuno-RNA FISH in THP-1 cells infected with HIV-1 ANCH3 (MOI 20) ±
1093 NEV (10 μM). The graph shows the average percentage per nucleus of vRNA found
1094 inside CPSF6 clusters, ± SEM (2 days p.i. = 56 cells, 151 vRNA (-NEV), 61 vRNA
1095 (+NEV); 3 days p.i. = 69 cells, 228 vRNA (-NEV), 129 vRNA (+NEV); 7 days p.i. = 45
1096 cells, 148 vRNA (-NEV); 57 vRNA (+NEV). **B)** Chromatin Immunoprecipitation of
1097 endogenous CPSF6 coupled to real-time PCR of different reverse transcription (RT)
1098 products in THP-1 cells infected with HIV-1 (MOI 5), 2 days p.i. ± SD. One-way ANOVA
1099 followed by Turkey's multiple comparison test, *=p ≤ 0.05, **=p ≤ 0.01, ****=p ≤ 0.0001.
1100 ChIP-CPSF6 products compared to the input in infected cells by western blot using an
1101 Ab anti-CPSF6. **C)** Confocal images of THP-1 cells infected with HIV-1 ANCH3 (MOI
1102 10) ± NEV (10 μM), 2 days p.i. Scale bars: 5 μm.

1103
1104 **Figure 6. HIV-1 proviruses locate outside HIV-1 MLOs. A)** Confocal images of THP-
1105 1 infected with HIV-1 ANCH3, 3 days p.i. The graph shows the intensity profiles of
1106 Hoechst, CPSF6 and SC35 signals along the segment crossing the MLO (yellow). **B)**
1107 Confocal images of THP-1 cells expressing OR-GFP infected with HIV-1 ANCH3, 3

1108 days p.i., compared to uninfected cells. On the right, the graphs show: the comparison
1109 of Pearson's r coefficients of SON-SC35 colocalization between infected and
1110 uninfected cells, per nucleus ($n = 25$ cells (HIV-1 ANCH3), 19 cells (NI); unpaired t
1111 test, ns = non-significant); the percentages of CPSF6 clusters associated to vDNA or
1112 to SC35 in 3D, per nucleus ($n = \text{CPSF6 clusters} > 50$); the distance of each vDNA from
1113 the closest SC35-speckle border ($n = 83$ vDNAs, 7 cells). **C)** Confocal images of THP-
1114 1 cells expressing MCP-GFP infected with HIV-1 ANCH3 MS2 (MOI 2.5), 3 days p.i.,
1115 \pm NEV (10 μ M). The graph shows the intensity profiles of Hoechst, MCP-GFP, CPSF6
1116 and SC35 signals along the segment crossing the MLO (yellow). **D)** Confocal images
1117 of THP-1 cells expressing MCP-GFP infected with HIV-1 ANCH3 MS2 (MOI 2.5), 3
1118 days p.i., compared to uninfected cells. The graph shows the percentages of CPSF6
1119 clusters associated to vRNA foci or to SC35 in 3D ($n = 42$ CPSF6 clusters, 8 cells) and
1120 the distance of each vRNA from the closest SC35-speckle border ($n = 31$ vRNAs, 8
1121 cells). **E)** Scatter plot with bars indicating the percentage of vDNA or vRNA associated
1122 to CPSF6, per nucleus in 3D ($n = 69$ vDNAs, 30 vRNAs, 8 cells). Unpaired t test, ns =
1123 non-significant. **F)** Scatter plot with bars indicating the distance of vDNA or vRNA from
1124 the border of the closest SC35/CPSF6 MLO ($n = 75$ vDNAs, 7 cells; 34 vRNAs, 8 cells).
1125 Unpaired t test, $**=p \leq 0.01$. **G)** Confocal image of Immuno-RNA FISH in THP-1 cell
1126 expressing OR-GFP infected with HIV-1 ANCH3 (MOI 20), 3 days p.i. Scale bar: 5 μ m,
1127 inset: 1 μ m.

1128
1129 **Figure 7. HIV-1 transcribes outside HIV-1 MLOs in primary MDMs.** Confocal
1130 images of Immuno-RNA FISH in primary MDMs infected with HIV-1 GFP (MOI 20) \pm
1131 NEV (10 μ M), 2-3 days p.i. The scatter plots show the GFP intensity per cell ($n = 22$ (-
1132 NEV) 20 (+NEV) cells) and the percentage of vRNA outside CPSF6 clusters per
1133 nucleus ($n = 22$ (-NEV) 20 (+NEV) cells; vRNAs: 268 (-NEV), 66 (+NEV)); unpaired t
1134 test, $****=p \leq 0.0001$. Their correlation in infected cells (Pearson's r coefficient) is
1135 displayed in the graph ($n = 22$ cells). The FACS histogram displays CD14+ expression
1136 of the MDMs. The FACS dot plot shows the correlation of GAG signal and GFP
1137 expression, with the related percentages per population. Scale bar: 5 μ m

1138
1139 **Figure 8. HIV-1 proviruses locate in LEDGF-enriched sites.** **A)** Confocal images of
1140 THP-1 cells expressing OR-GFP infected with HIV-1 ANCH3, 3 days p.i., compared to
1141 uninfected cells. The scatter plots show the percentages of CPSF6 found associated

1142 to LEDGF clusters per nucleus in 3D (n = 16 cells; unpaired t test, ***=p ≤ 0.001) and
1143 the LEDGF and CPSF6 count per nucleus in 3D (n = 16 cells); unpaired t test, ns =
1144 non-significant, ****=p ≤ 0.0001. Scale bar: 5 μm, inset: 2 μm. **B)** Confocal images of
1145 THP-1 cells expressing OR-GFP infected with HIV-1 ANCH3 and expressing MCP-
1146 GFP infected with HIV-1 ANCH3 MS2. The scatter plot shows the percentage of vDNA
1147 or vRNA associated to LEDGF in 3D (n= 33 (vDNA), 15 (vRNA)) ± SD. Unpaired t test,
1148 ns = non-significant. The pie charts show the percentages of the 2 populations of
1149 LEDGF clusters associated to vDNA or vRNA: LEDGF alone or LEDGF in proximity of
1150 CPSF6. Scale bar: 5 μm, inset: 1 μm.

1151

1152 **Figure 9. Remodeling of the nuclear landscape by HIV-1 to replicate.** New, refined
1153 model of viral intranuclear steps. Upon infection, HIV-1 triggers the formation of CPSF6
1154 clusters which localize in nuclear speckles (NSs) (marked by SC35) forming HIV-1
1155 MLOs, which retain viral genomic RNA and integrase proteins. HIV-1 MLOs are sites
1156 of the reverse transcription and of the HIV-1 PIC maturation. Once the mature PIC is
1157 formed, it leaves the CPSF6 cluster to proceed with the integration step. HIV-1
1158 integration occurs in active chromatin regions enriched in LEDGF, close to the nuclear
1159 envelope and to HIV-1 MLOs. Indeed, HIV-1 replication might be favored for viral post-
1160 transcriptional processing by the proximity to NSs that host splicing factors. IN,
1161 Integrase; gRNA, viral genomic RNA; PIC, Pre-Integration Complex; NPC, Nuclear Pore
1162 Complex; vRNA, viral RNA; LTR, Long Terminal Repeat. Created with BioRender.com.

1163

A

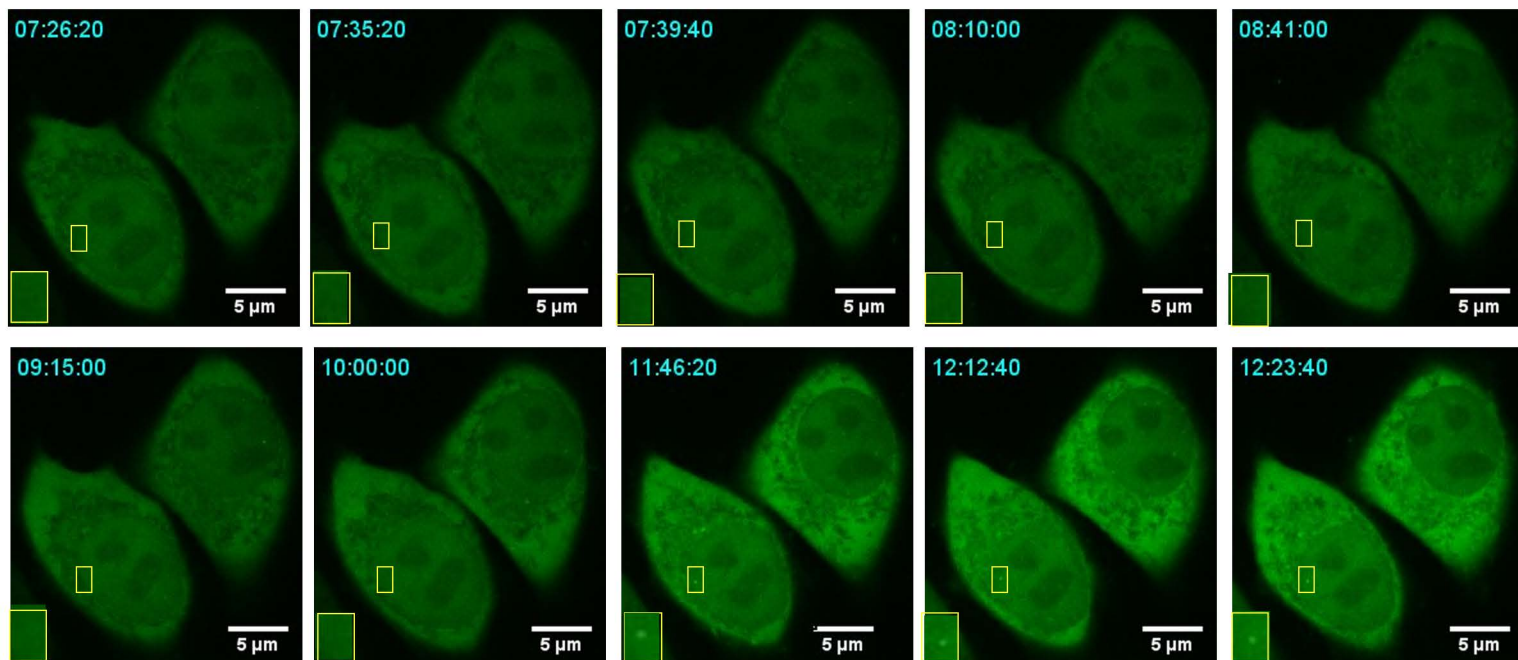
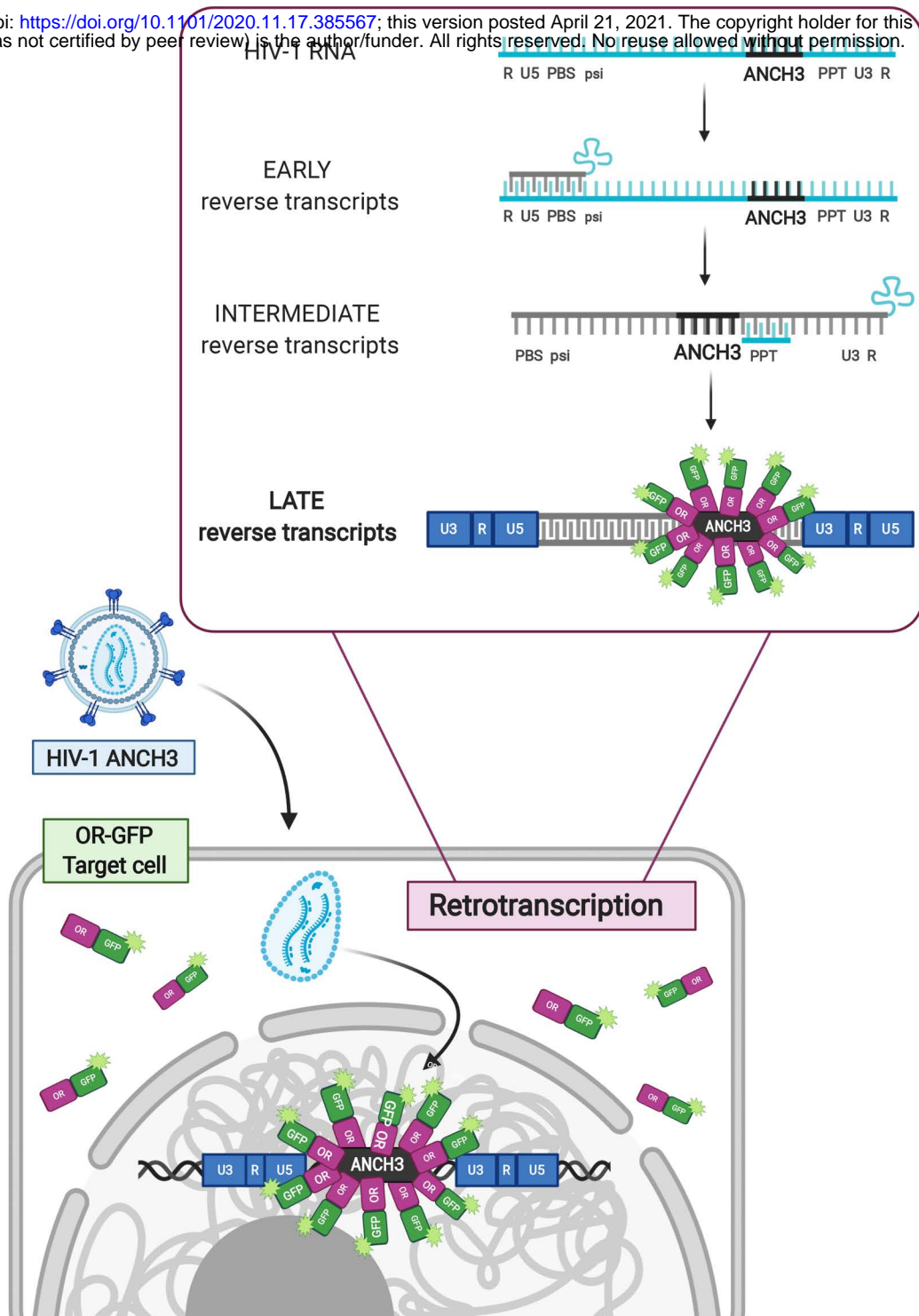
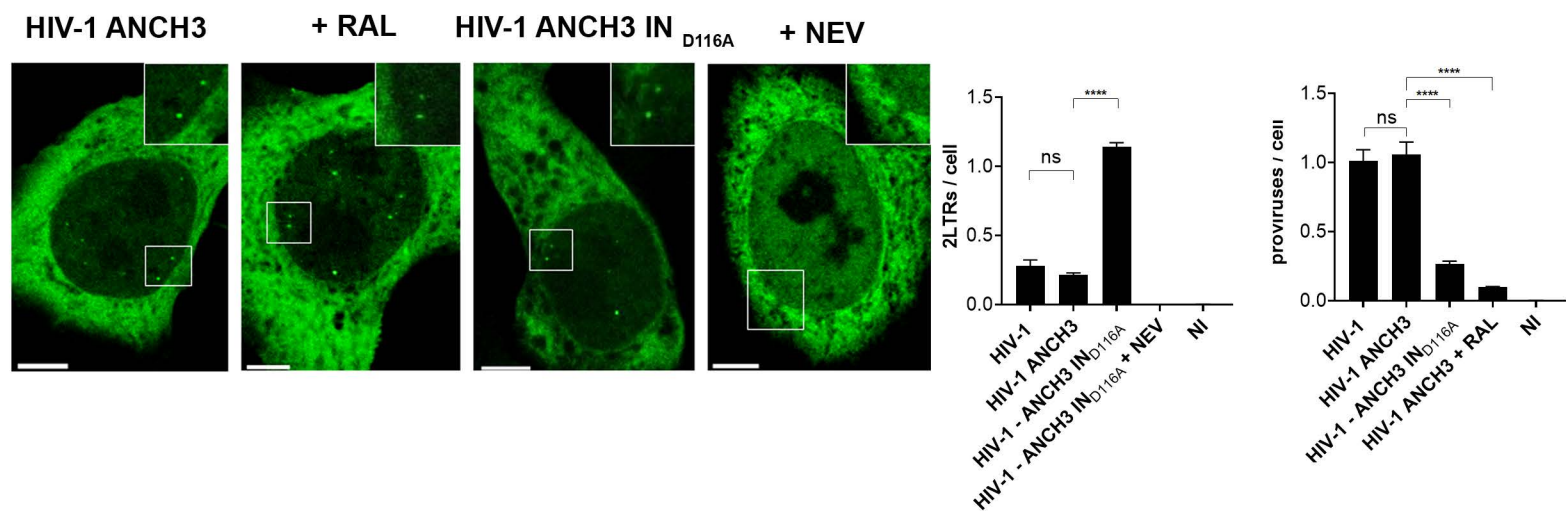
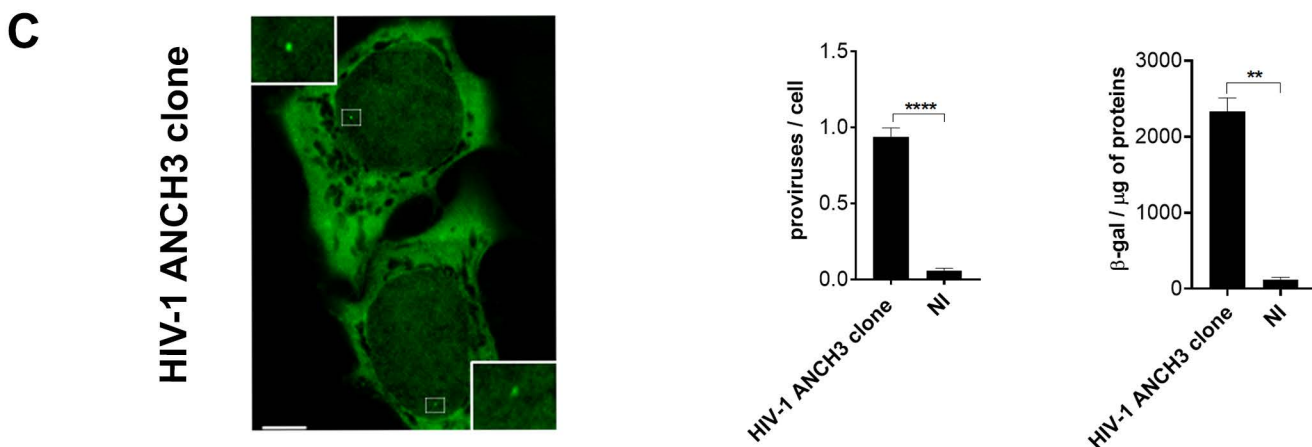


Figure 1

B



C



D

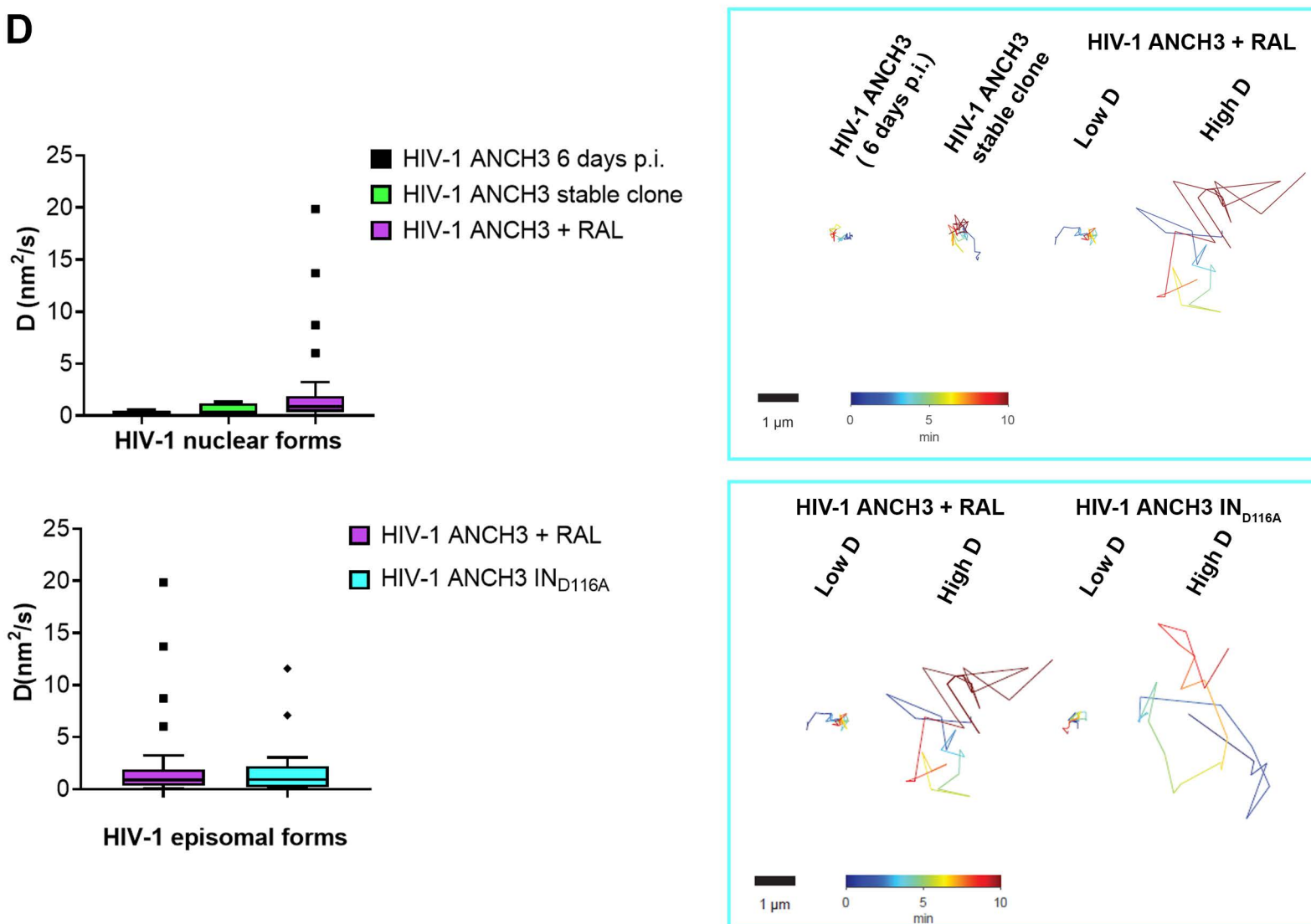
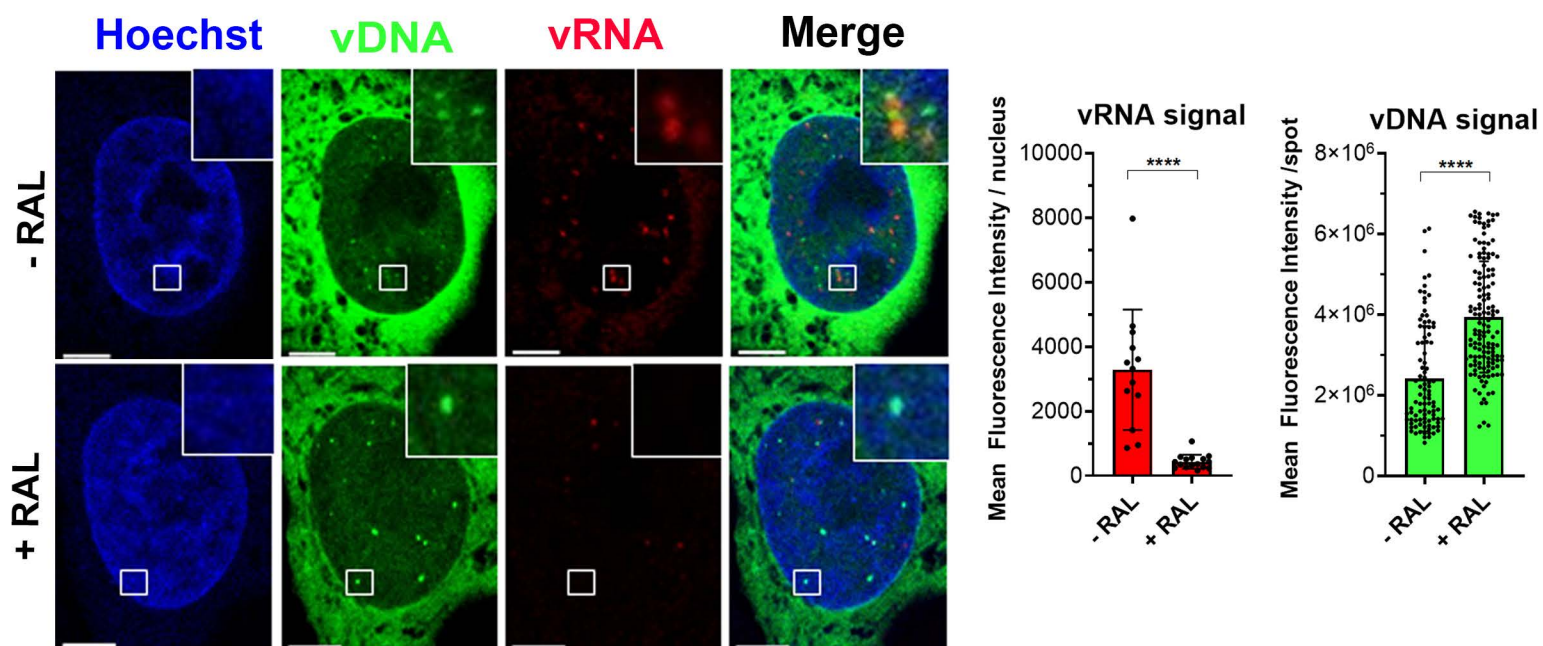


Figure 1

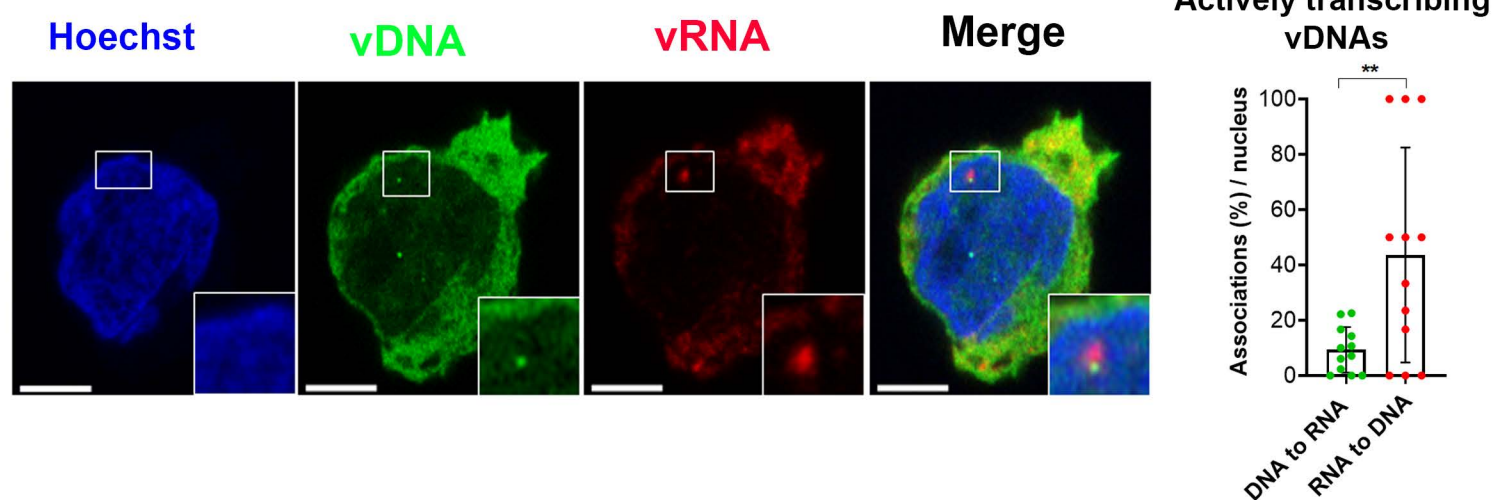
A

HeLa cells



B

CD4+ T cells



C

THP-1 cells

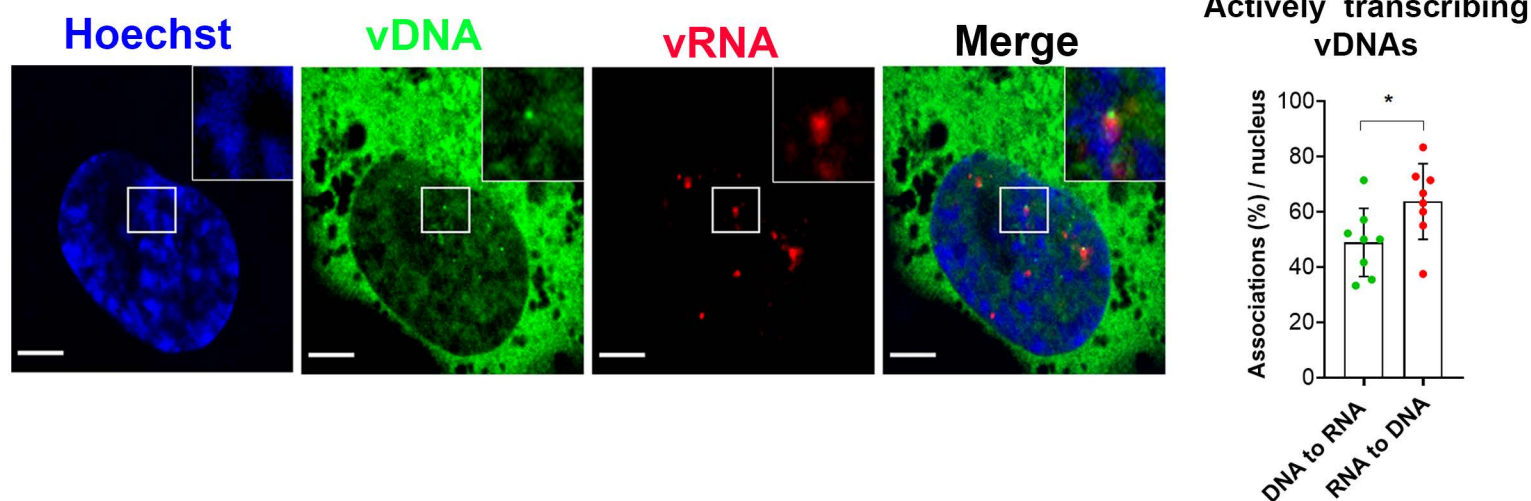
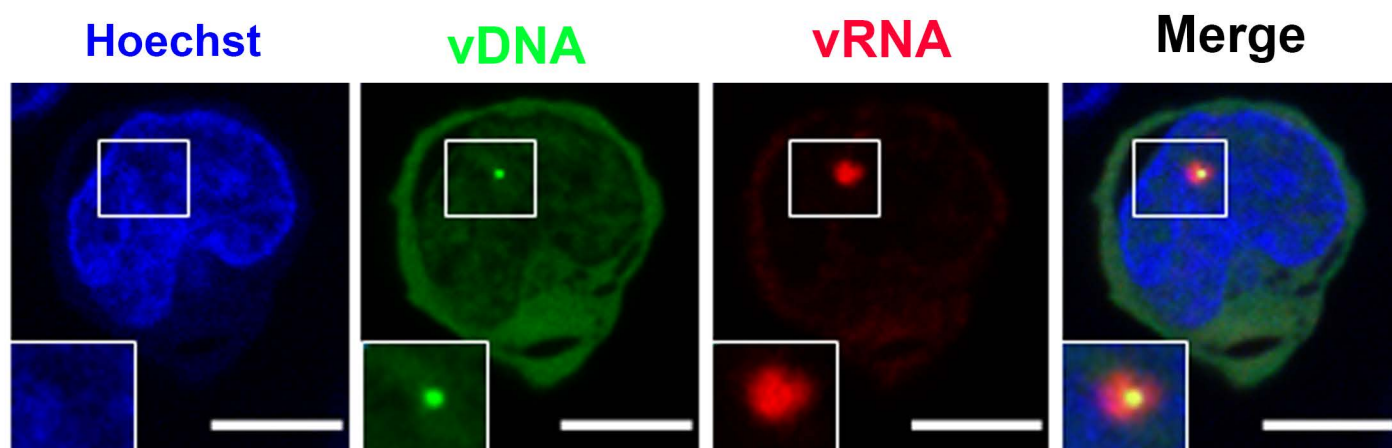


Figure 2

D

Primary CD4+ T cells



Primary macrophages

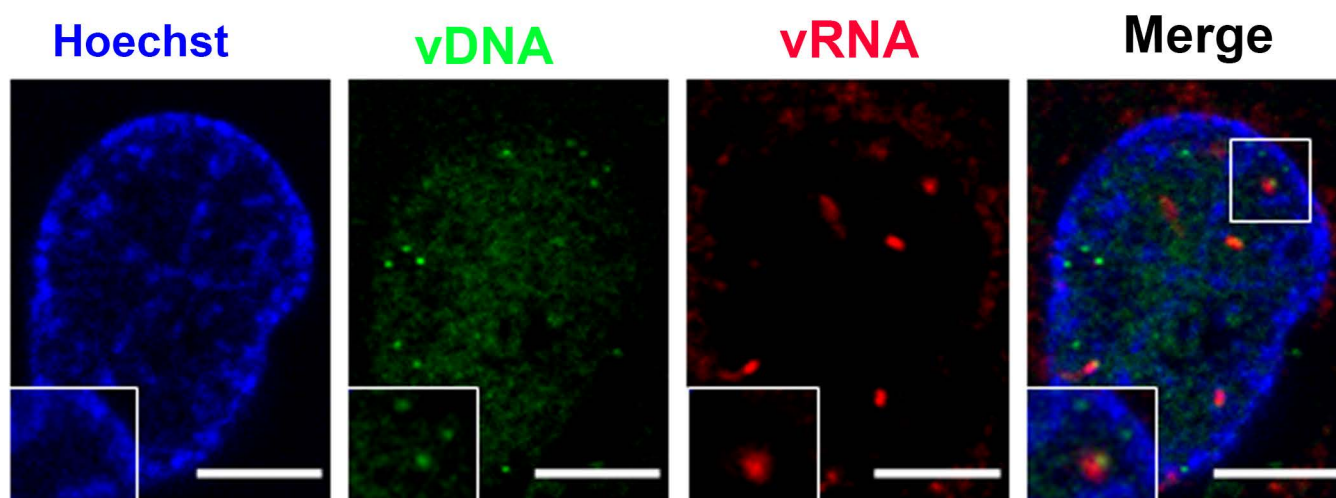
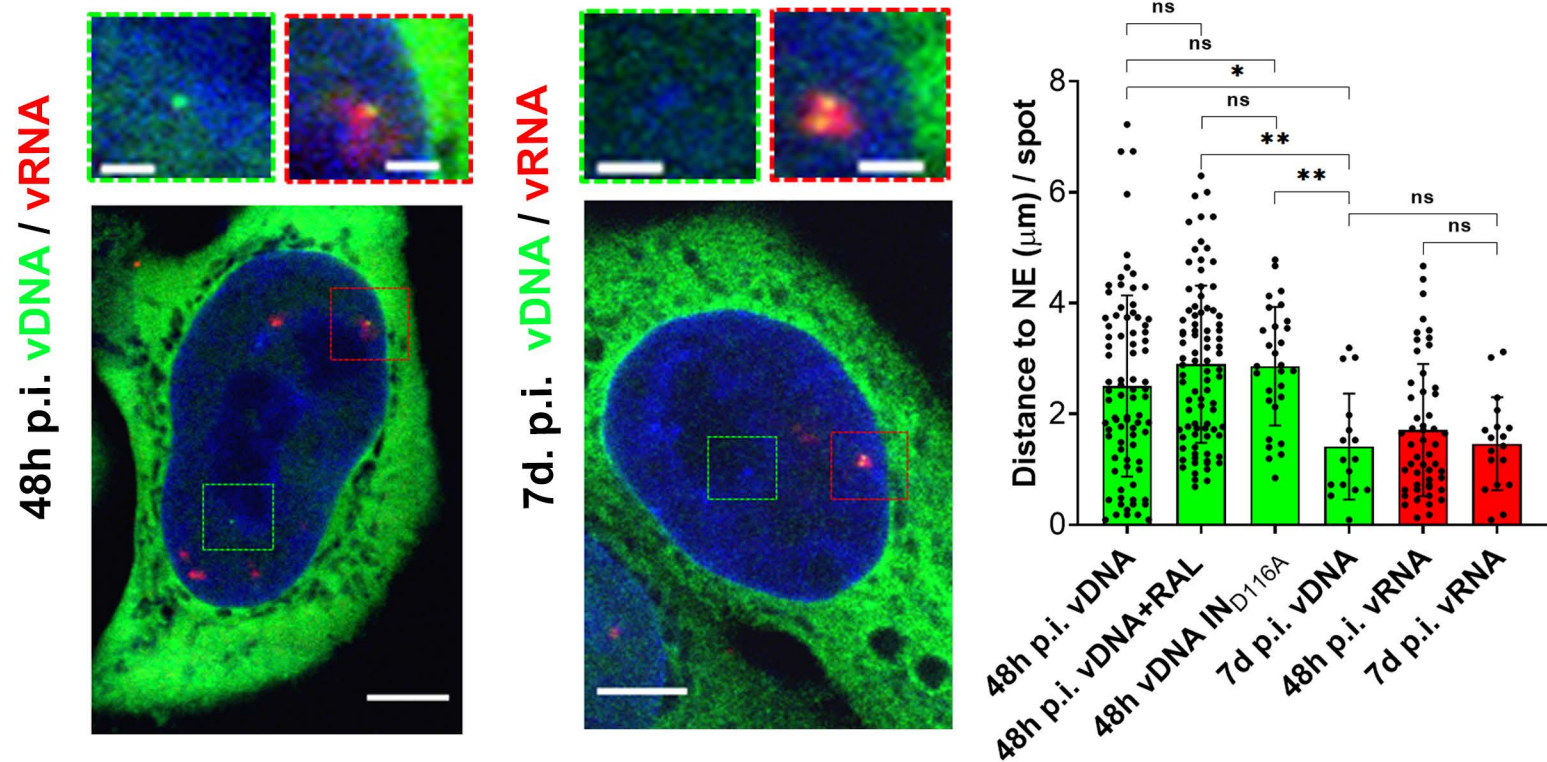


Figure 2

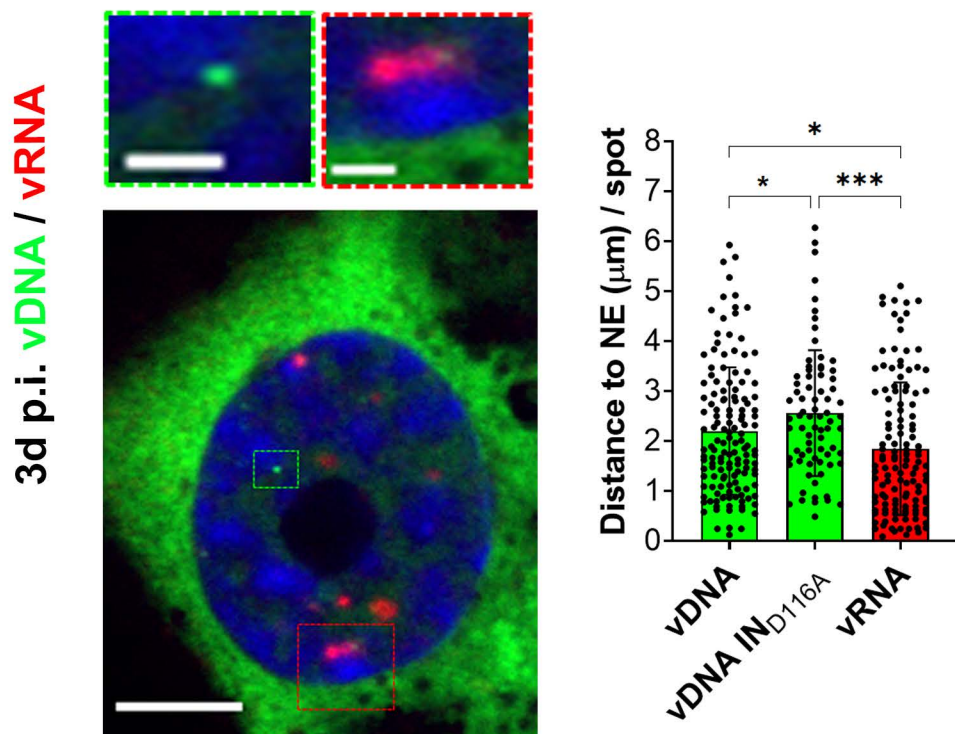
A

Dividing cells: HeLa



B

Non-dividing cells: THP-1



C HeLa vs THP-1

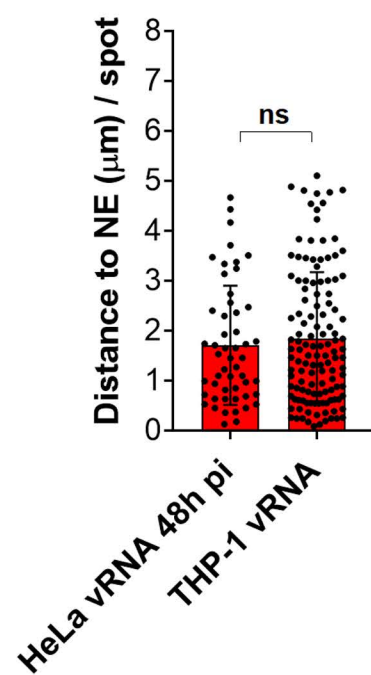


Figure 3

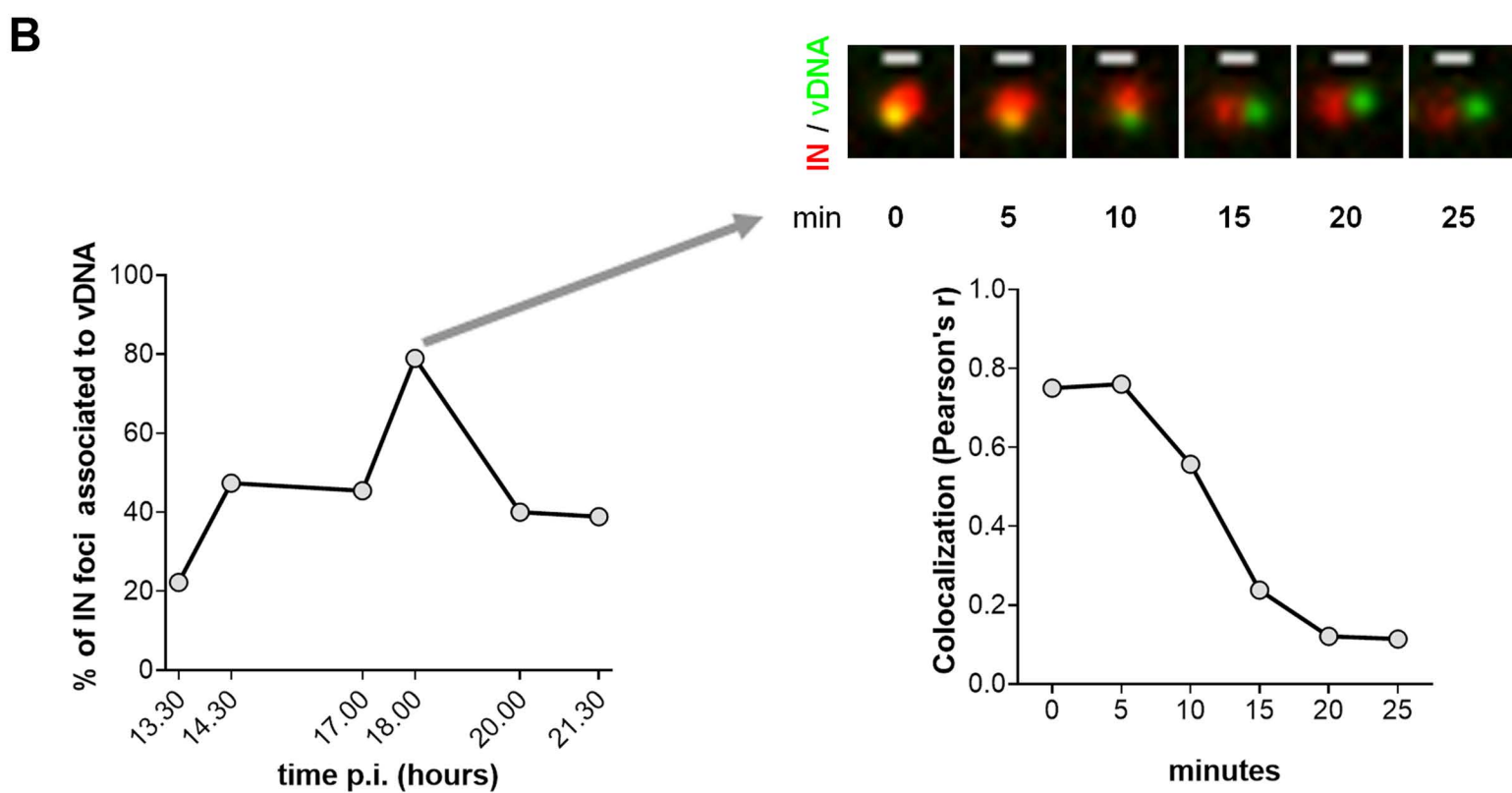
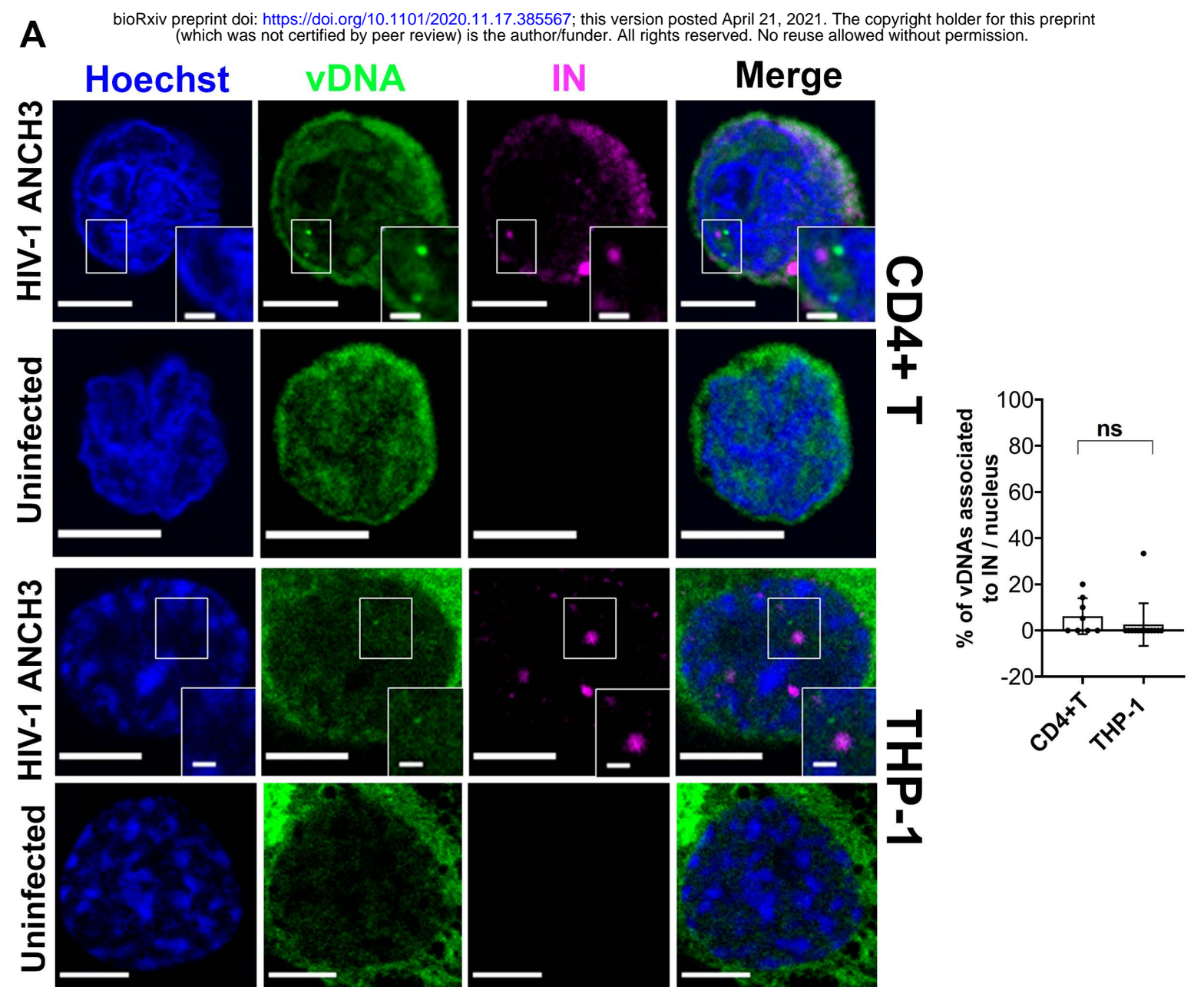


Figure 4

C

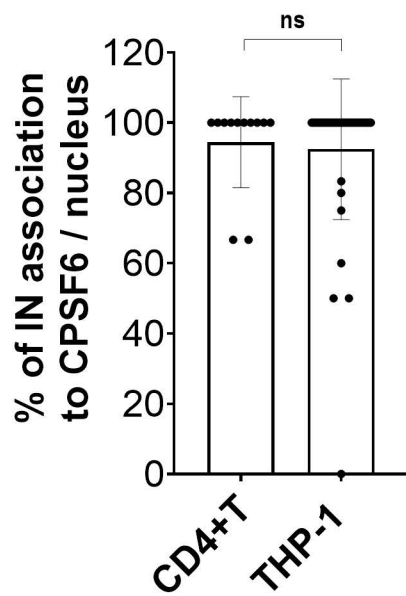
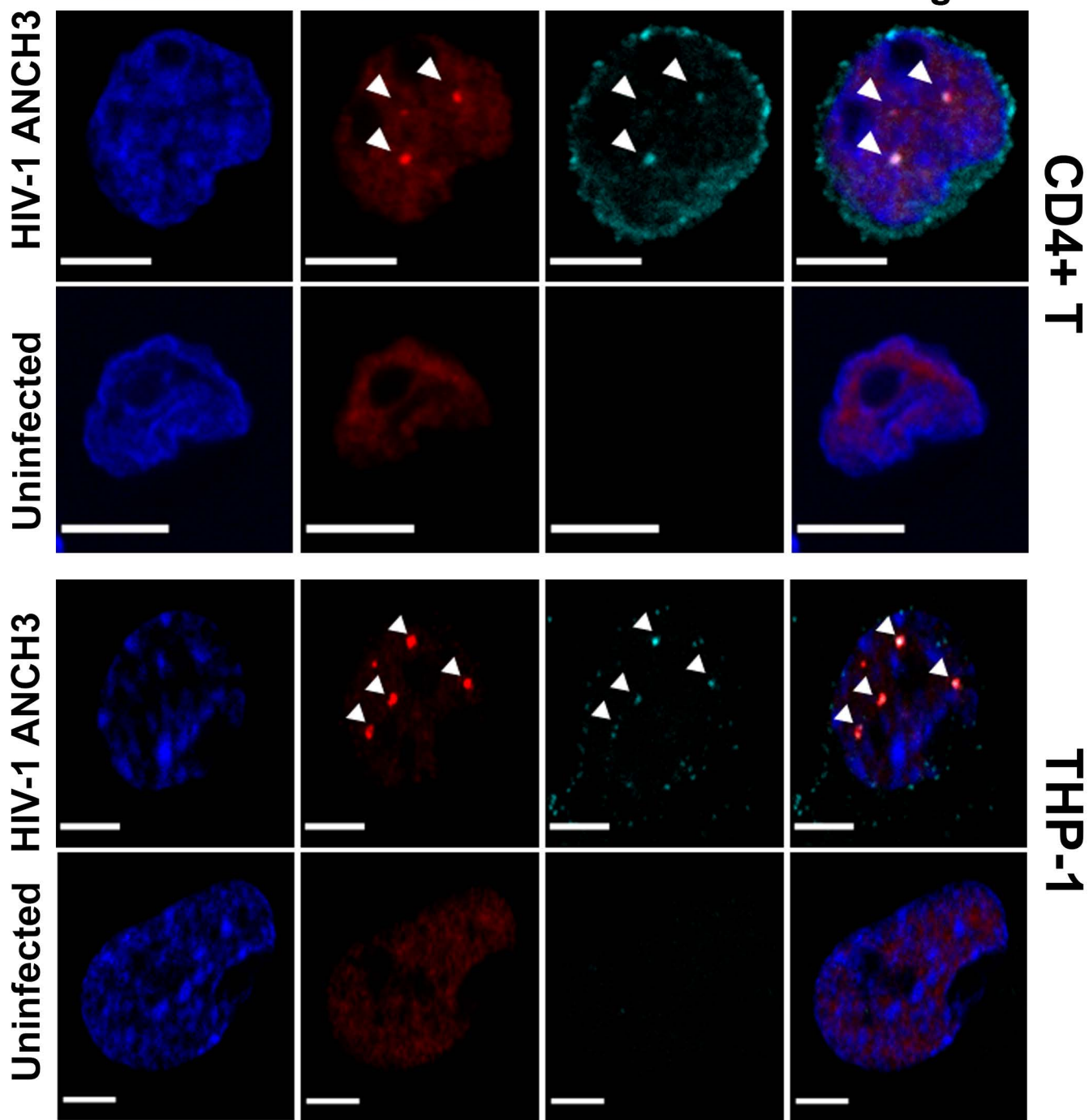


Figure 4

D

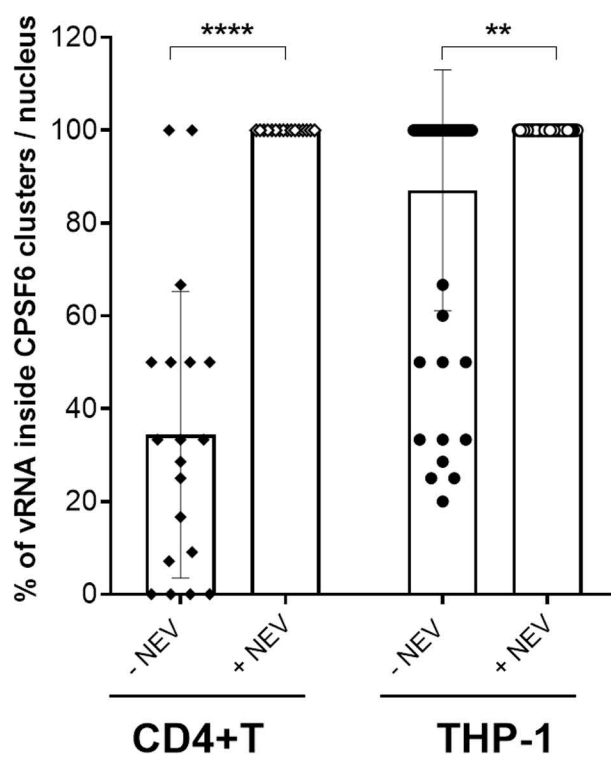
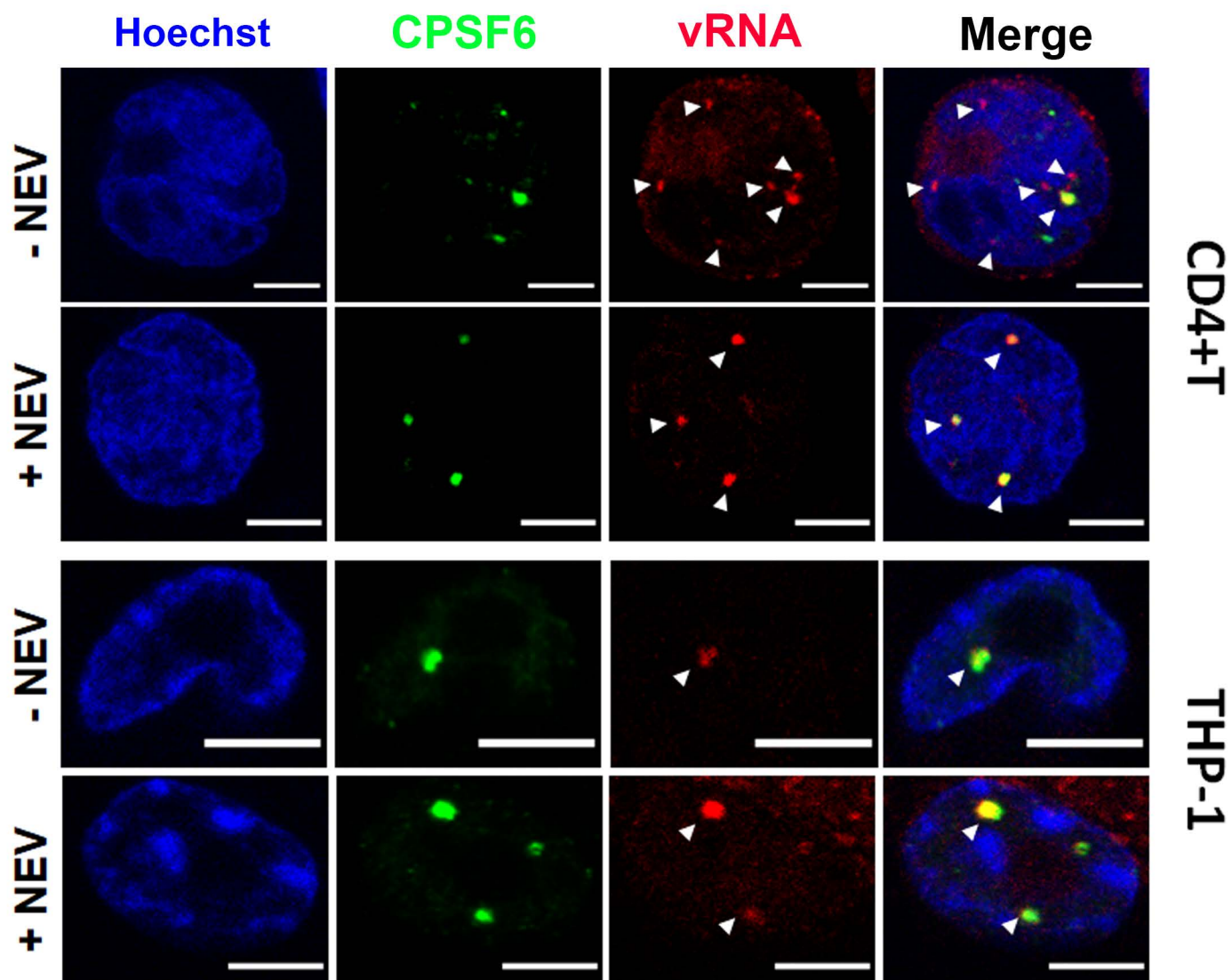
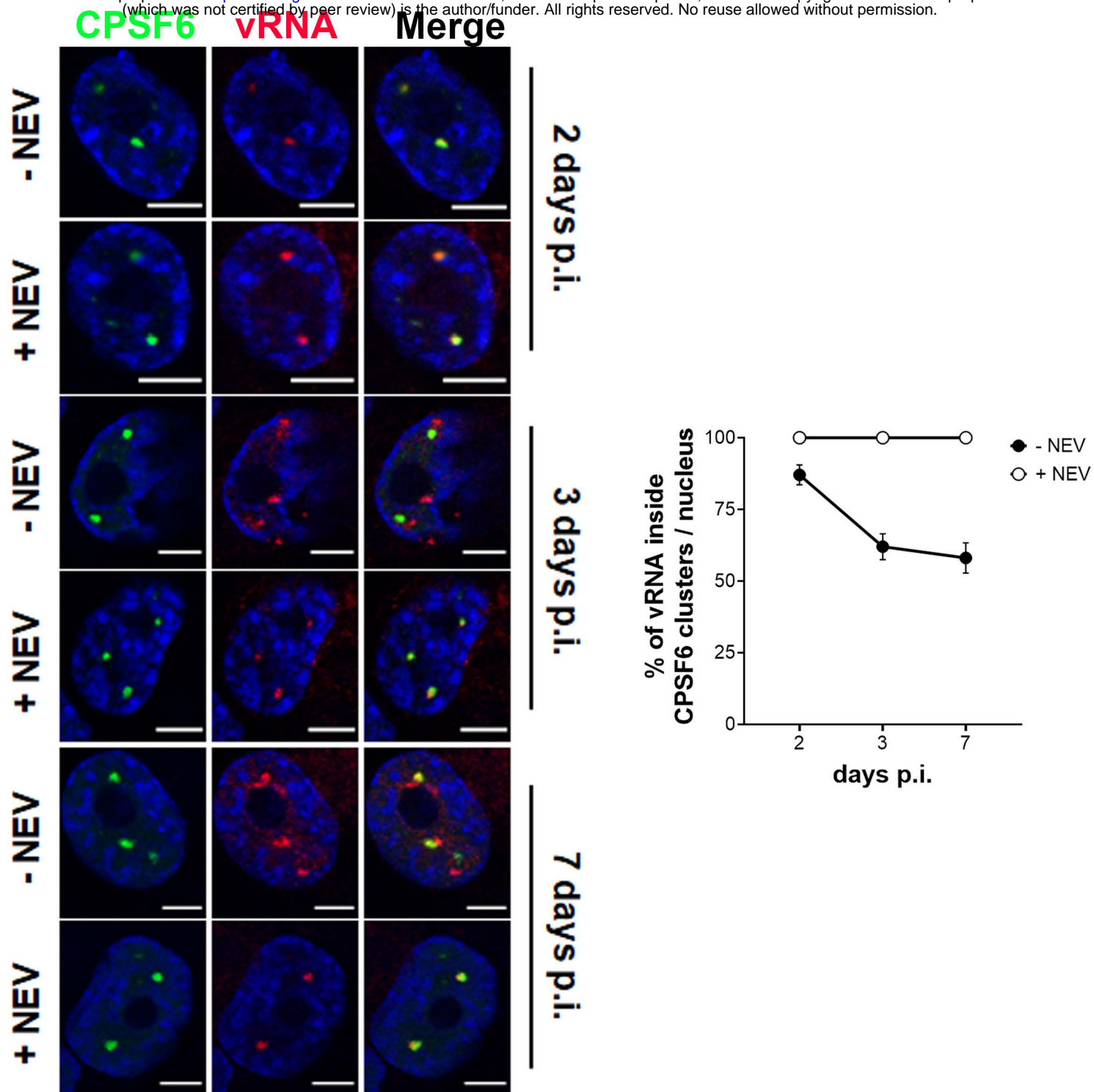


Figure 4

A



B

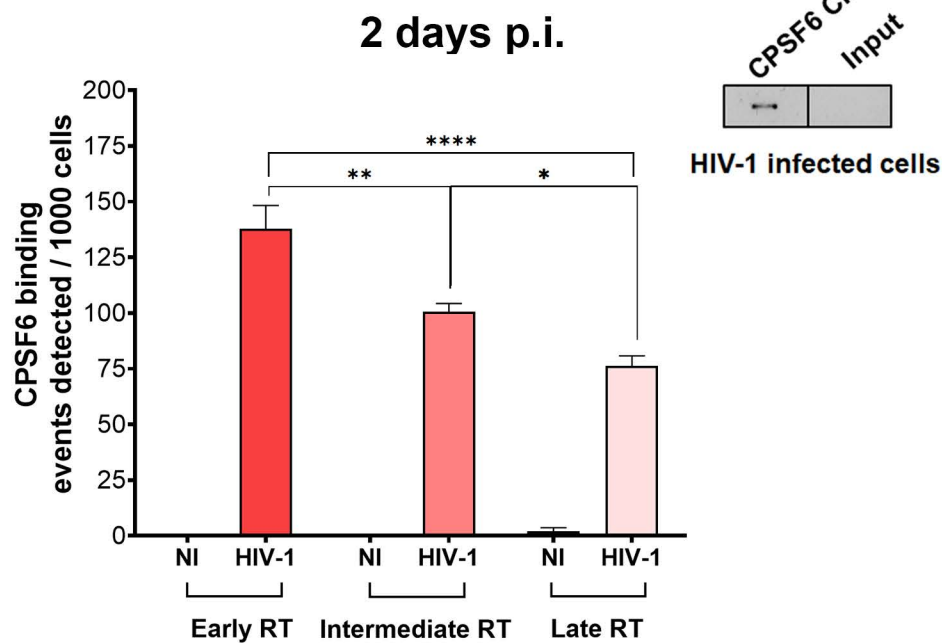


Figure 5

C

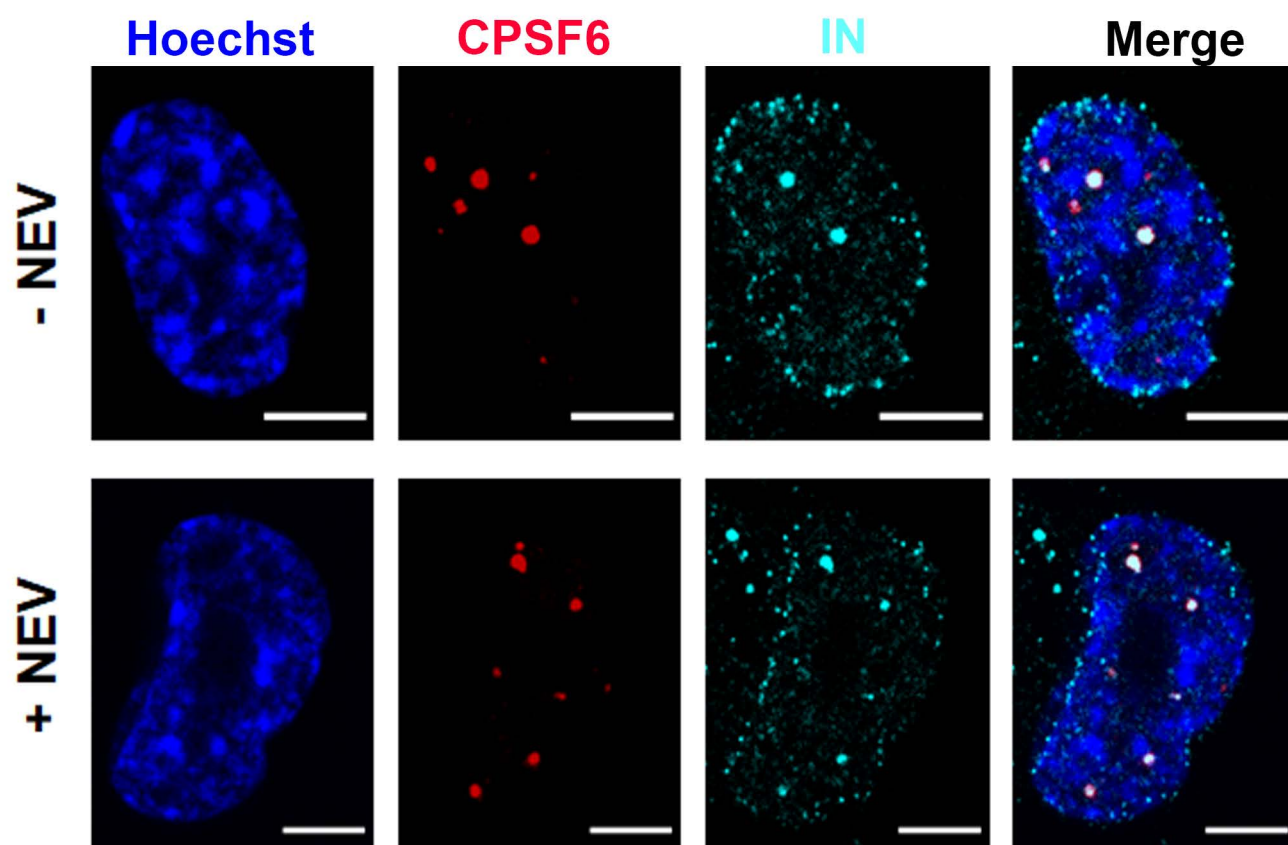
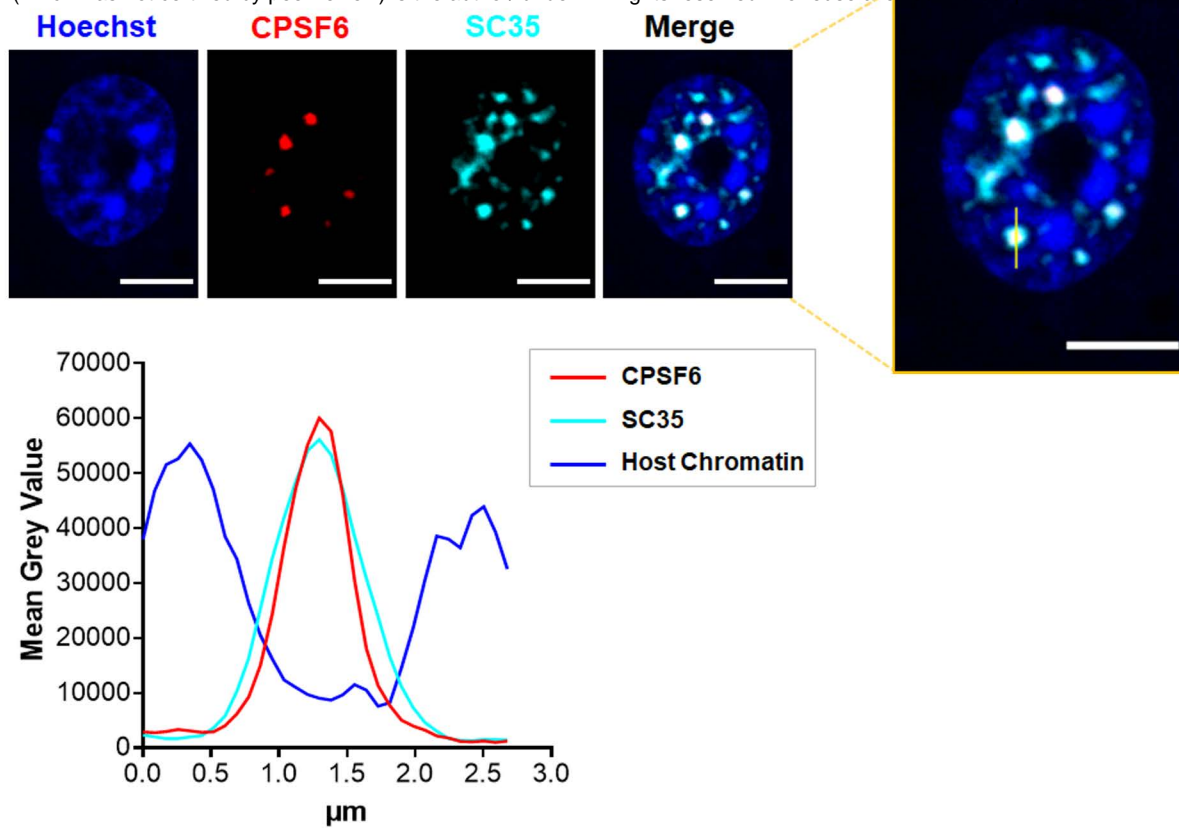


Figure 5

A



B

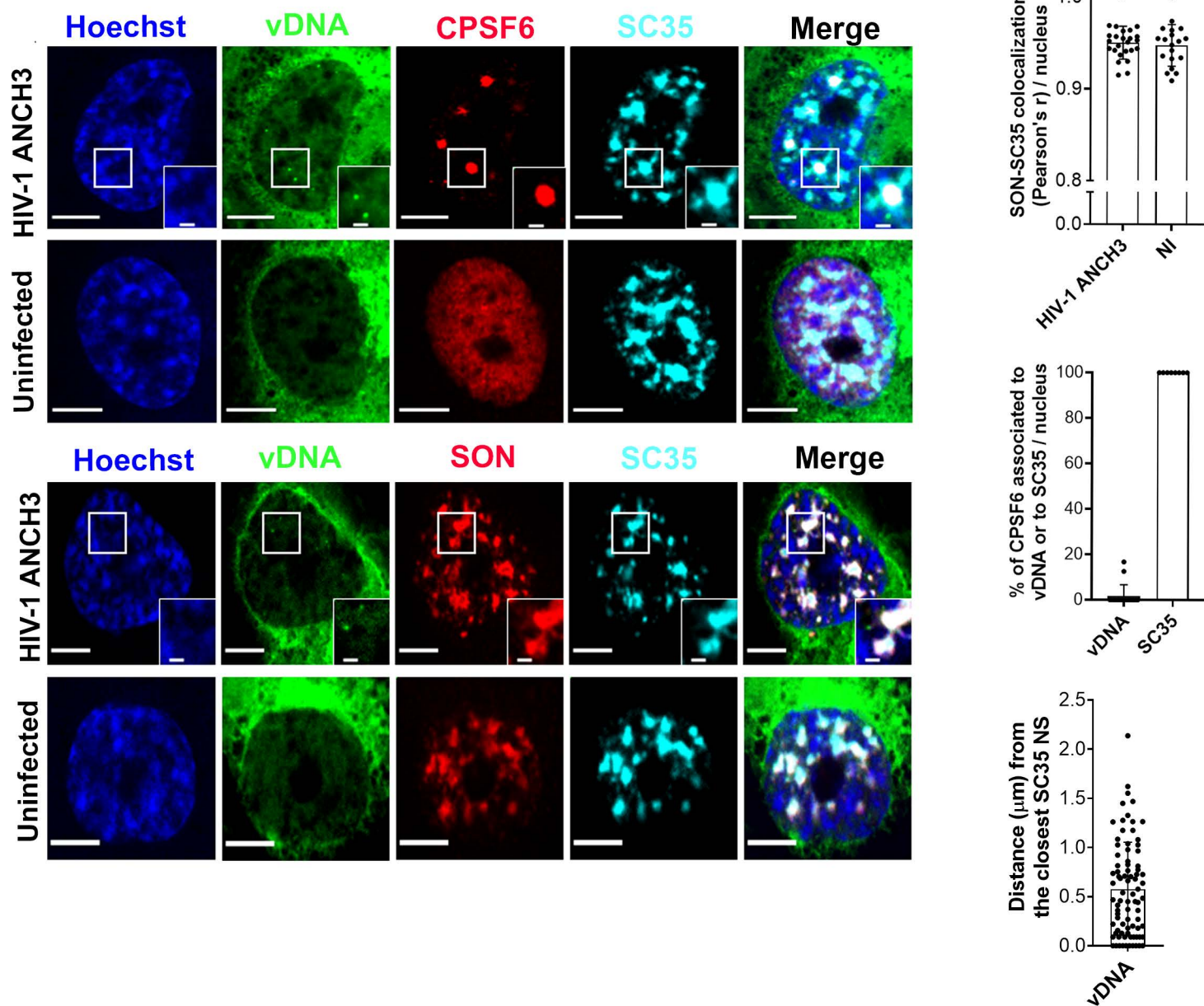


Figure 6

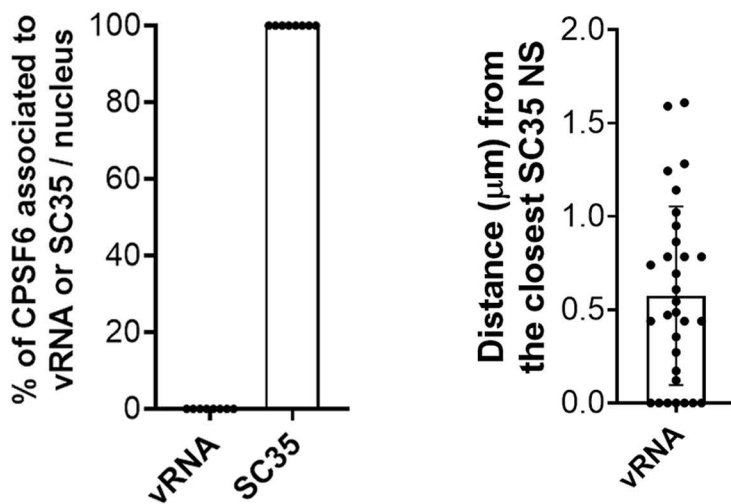
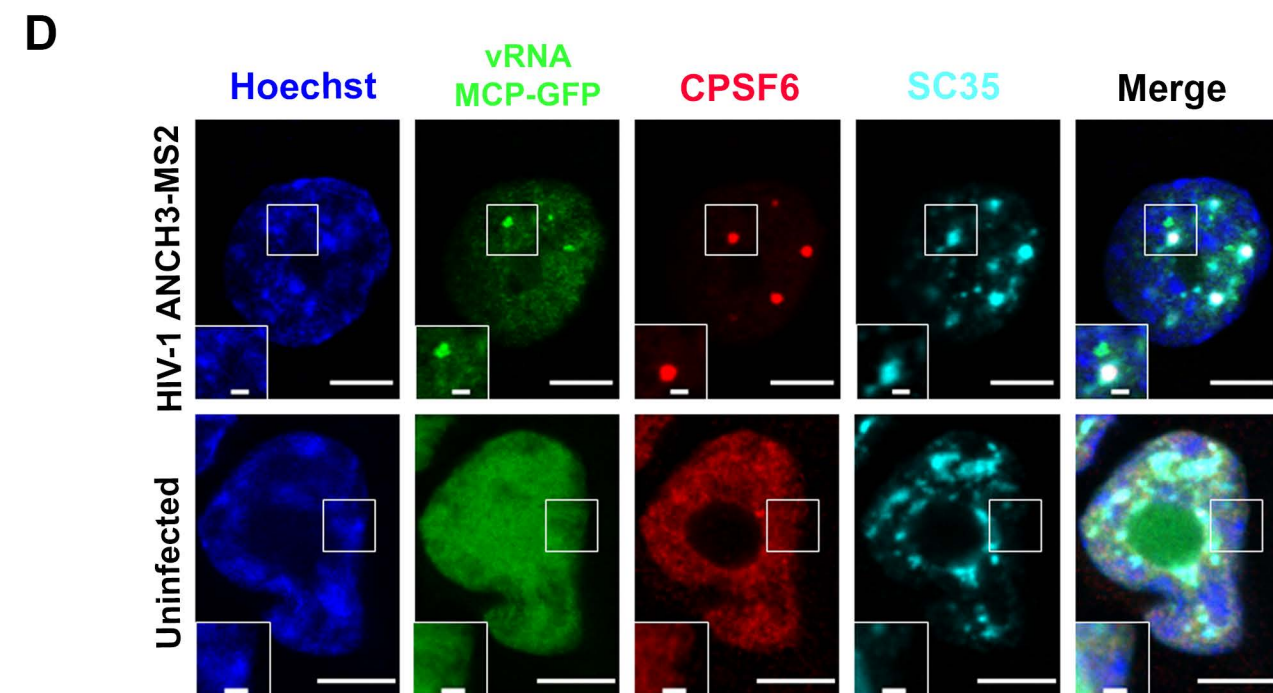
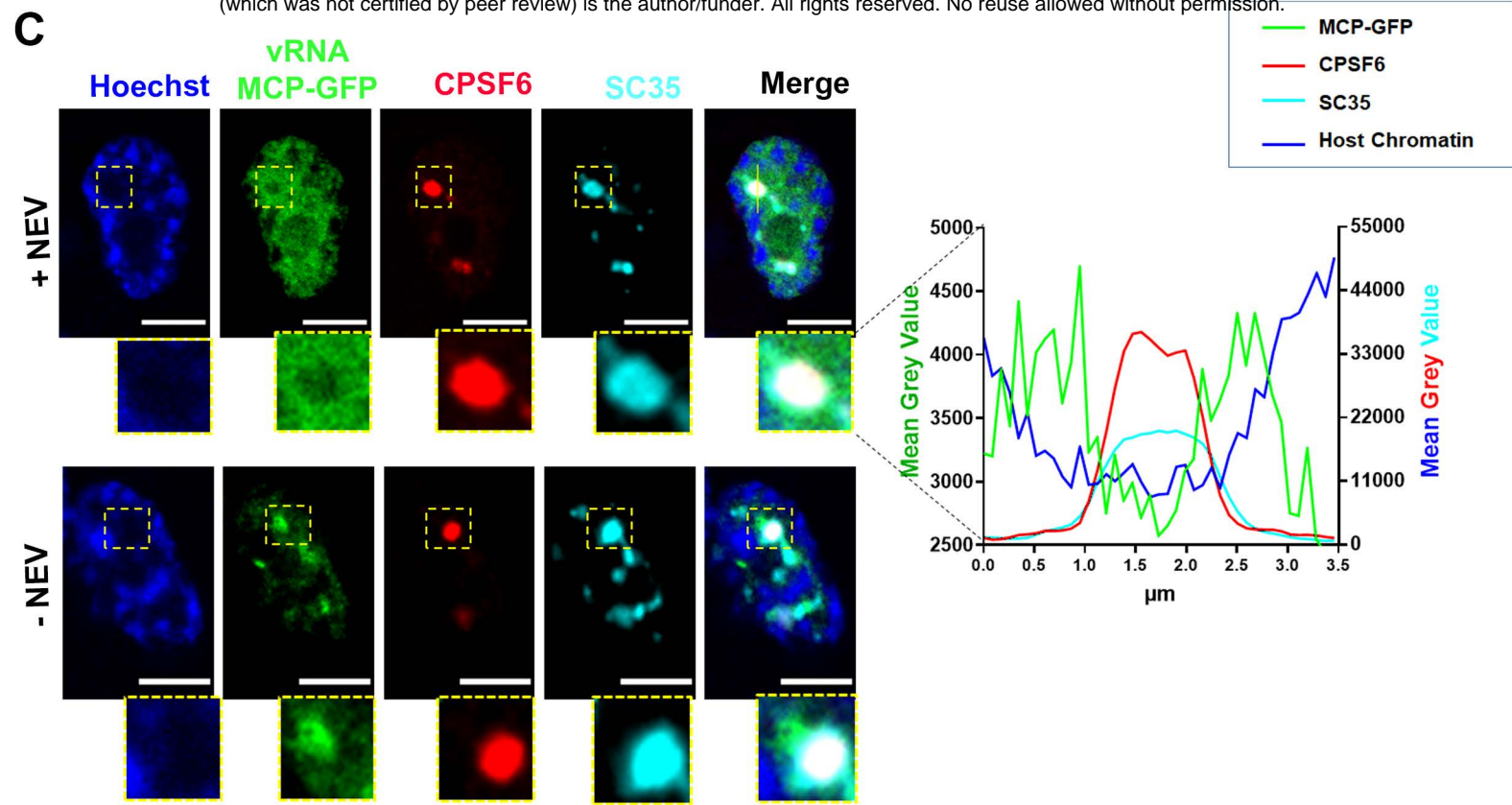
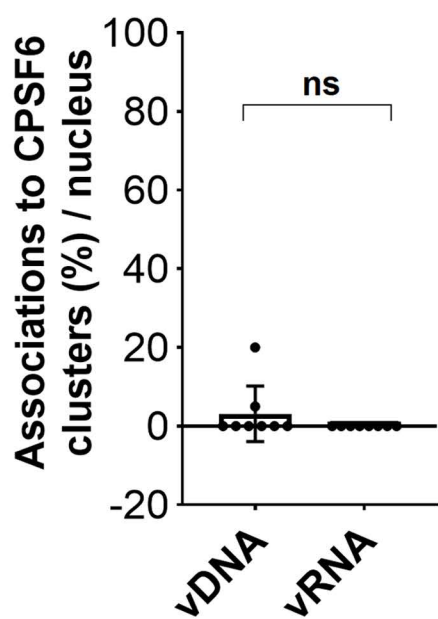
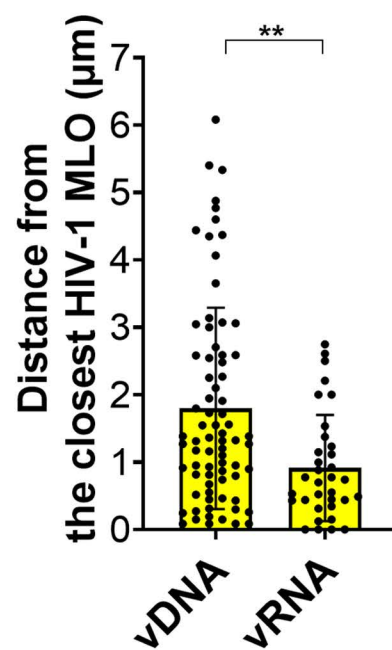


Figure 6

E



F



G

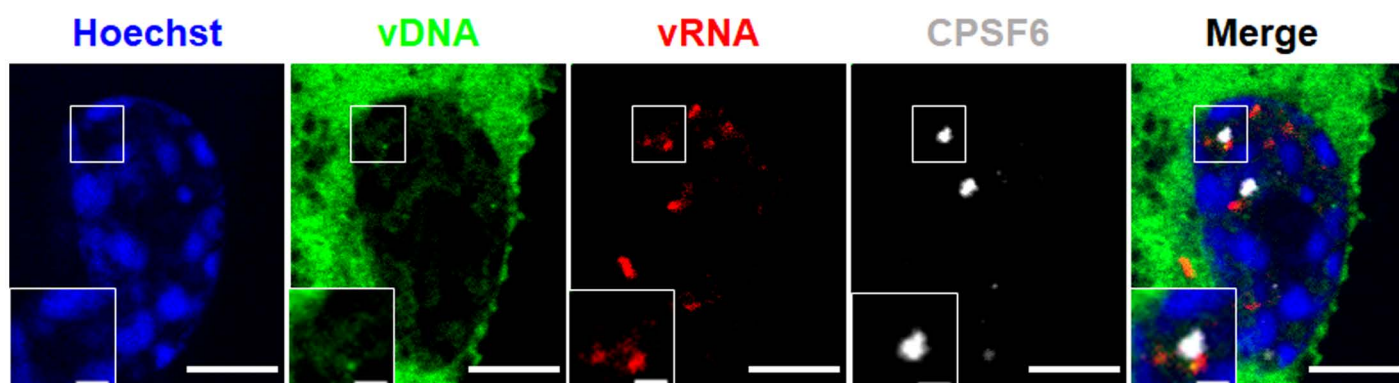


Figure 6

MDM 3 days p.i.

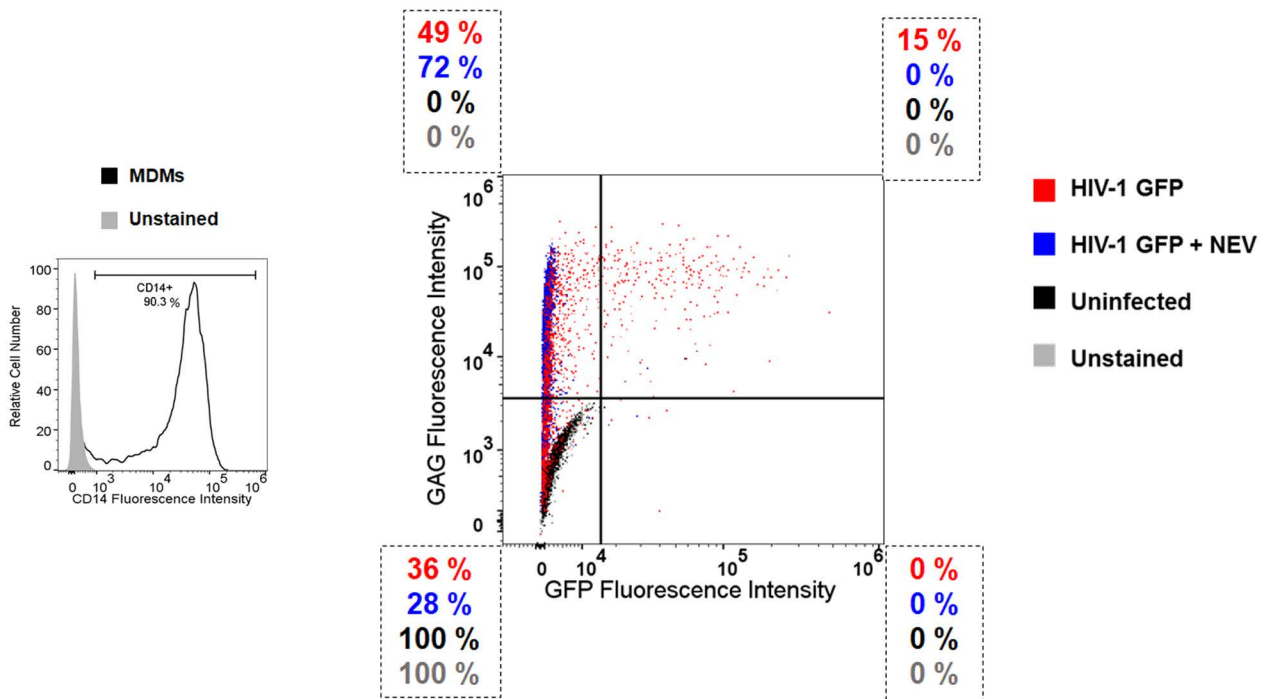
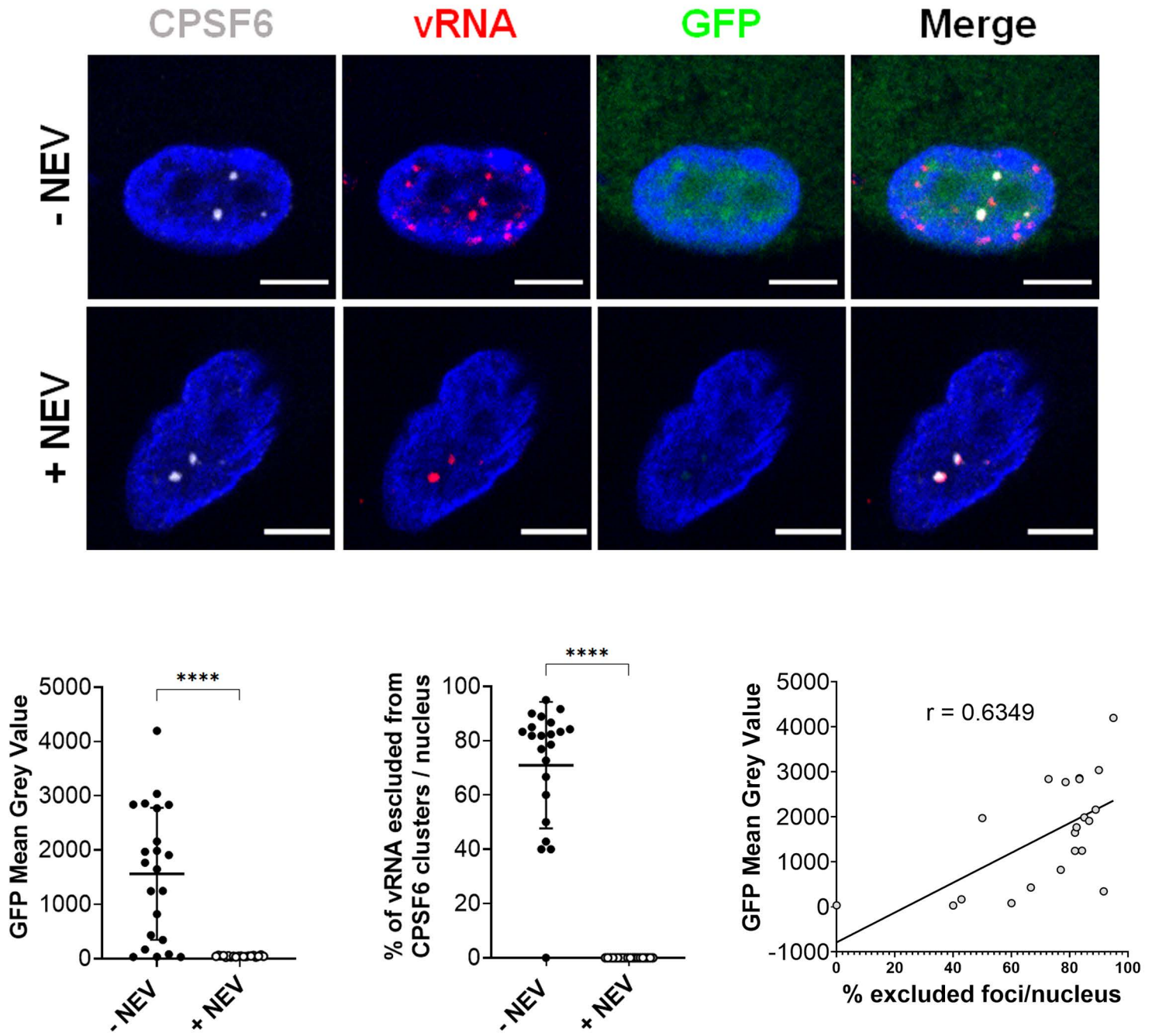
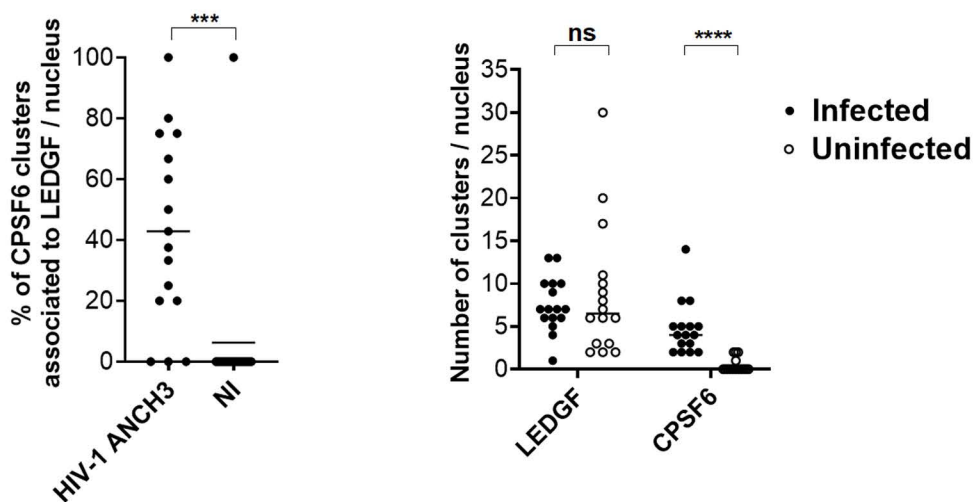
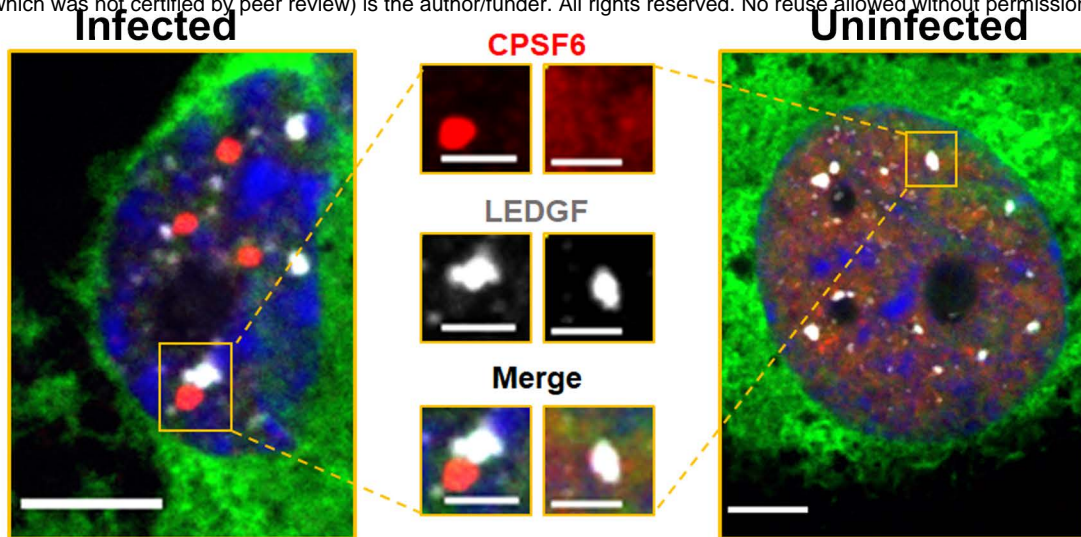


Figure 7

A



B

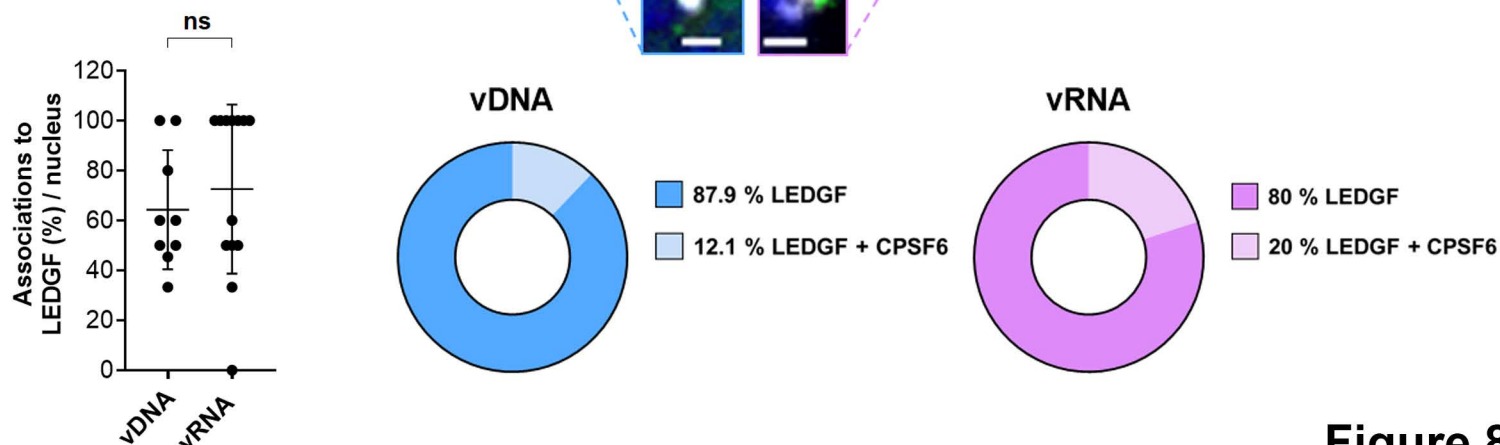
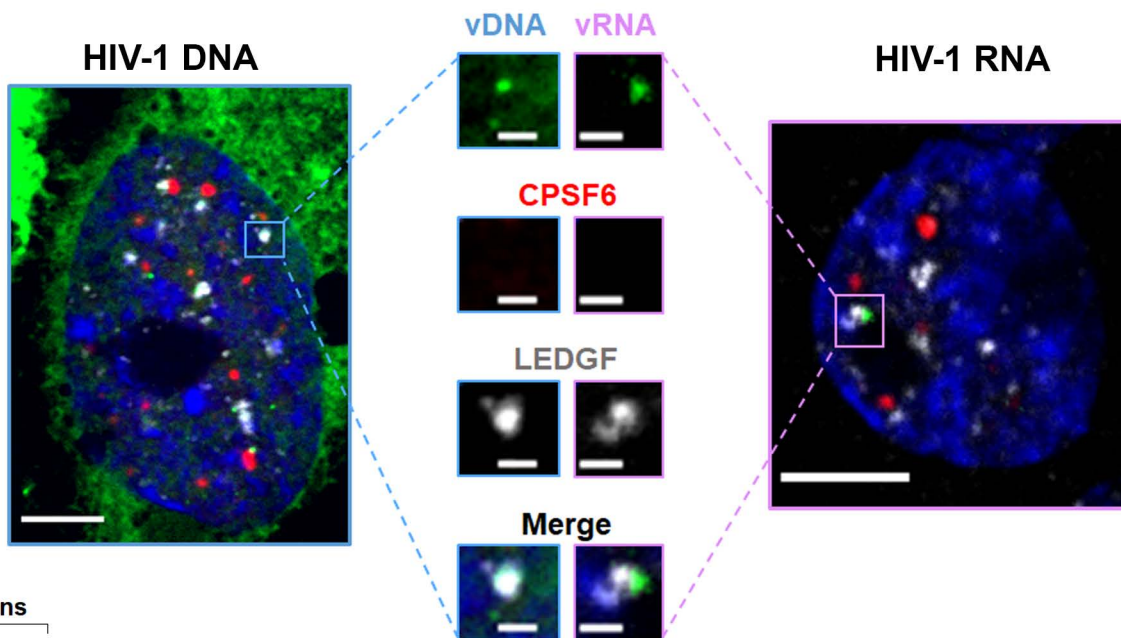


Figure 8

Uninfected

Infected

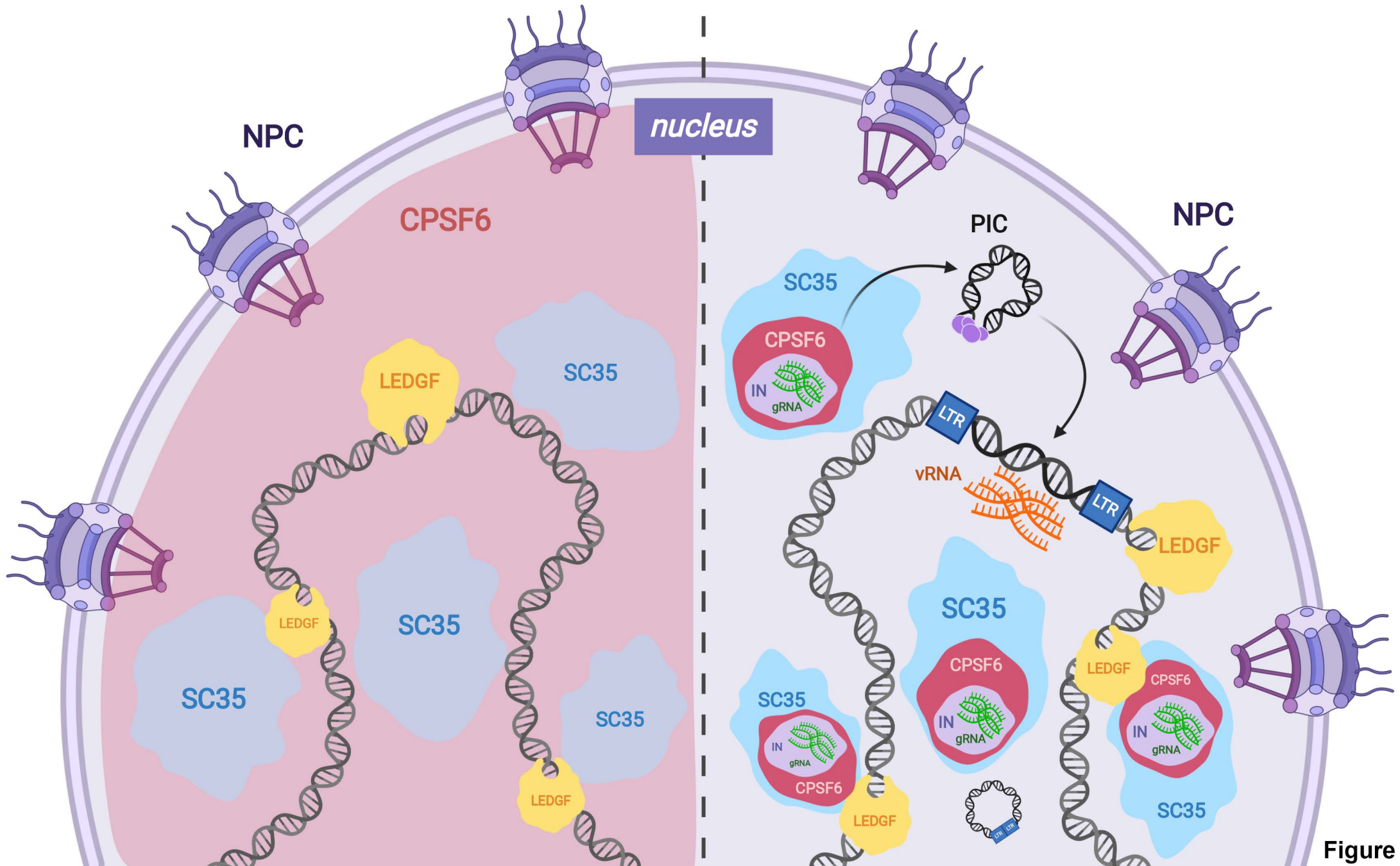


Figure 9